Journal of Computational Physics **182,** 301–336 (2002)
doi:10.1006/jcph.2002.7169

Reconstruction of Turbulent Fluctuations Using a Hybrid RANS/LES Approach

E. Labourasse and P. Sagaut[1]

ONERA, CFD & Aeroacoustics Department, 29 av. Division Leclerc, 92 Châtillon, France
E-mail: sagaut@onera.fr

Received January 26, 2001; revised June 27, 2002

A hybrid RANS/LES approach is presented and assessed considering several flows, which can be interpreted as the most general case of the NLDE approach as defined by Morris *et al*. [P. J. Morris, L. N. Long, A. Bangalore, and A. Wang, *J. Comput. Phys.* **133**, 56 (1997)]. A decomposition into three parts of the exact solution of the Navier–Stokes equations is considered: mean flow, resolved fluctuations, and unresolved (subgrid) fluctuations. The mean flow is computed using a classical RANS method, while resolved fluctuations are derived from a LES method. This approach is succesfully assessed on the stationary and the pulsed plane channel flow configurations. The case of the flow around a low-pressure turbine blade is discussed in a second step. The hybrid method is also demonstrated to be robust with respect to several sources of error and provides good results in the case of a coarsened grid simulation, a reduced computational domain simulation, and nonconsistent mean flow fields.

Key Words: Navier–Stokes equations; Reynolds averaged Navier–Stokes; large eddy simulation; turbulence.

1. INTRODUCTION

Unsteady simulation of turbulent flows is of great interest for many applied and theoretical purposes. But even using the most powerful supercomputers, direct simulation of all the turbulent motions is still out of range when high-Reynolds-number flows are considered. Because these flows are of great importance, some ways to describe the unsteadiness associated with turbulent fluctuations at lower costs than for the direct simulation approach must be defined.

Two classical approaches have been widely used during the last decades: unsteady Reynolds averaged simulation (URANS), which relies on an ensemble average of the exact

[1] Fax: (33) 1 46 73 41 66.

0021-9991/02 $35.00

solution, and large-eddy simulation (LES), which is based on a low-pass filtering of the solution (see Refs. [16, 19, 33] for a review). The former is known to give some information on the motion of coherent structures, whose definition can be related to the one of a conditional average, and does not incorporate explicitely a cutoff frequency. This approach takes advantage of the enormous amount of work devoted to the development of turbulence models for steady RANS computations (see Ref. [26] for a review) and can be used to study flows at high Reynolds number in complex geometries. The latter approach makes it possible, because it is based on an explicit cutoff frequency, to choose the degree of accuracy of the description of turbulent fluctuations. A well-known drawback of LES when engineering applications are aimed at is that driving mechanisms, i.e., physical mechanisms which are responsible for turbulence production, must be resolved and the computational grid has to be defined in consequence. When driving mechanisms are not correctly represented in the computation, LES is known to exhibit dramatic errors: turbulence is badly predicted, leading to significant errors in the mean field. Because very fine meshes are often needed to capture these mechanisms, LES cannot yet be considered a general engineering tool, and new ways to use the filtered approach have to be defined.

The approach presented in this paper is a trial that combines both RANS and LES approaches in order to take advantage of both methods. The idea consists of predicting the mean flow field with the RANS approach, which is less expensive and thus can be more easily optimized than LES to get accurate results on the mean velocity field, while locally reconstructing the unsteady turbulent motion with a LES-type simulation in subdomains. The expected gain with respect to the classical LES approach is twofold. First, given the mean field being prescribed, the errors commited on turbulent fluctuations will not pollute it, and we can expect this method to be more robust than classical LES. Second, if the turbulence-producing events are localized in a small region, it is possible to restrict the LES-type computation to a small sudomain included in the global domain, while classical LES would require consideration of the full domain.

Other coupled RANS/LES approaches can be derived, which are not considered in the present paper: hybrid multidomain computations, based on a zonal use of RANS and LES (see Refs. [28, 34]), or simulations relying on "universal models," which are able to operate the switch from RANS to LES. Examples of universal models are the two-part model based on the original work of Schumann (see Ref. [36]), the detached eddy simulation of Spalart *et al*. [41], the rescaled RANS approach first proposed by Speziale [42], and the hybrid dynamic model developed by Germano [5].

In some previous work relying on the same concept of reconstruction of fluctuations, using unsteady computations around a mean flow field has already been proposed, mainly for studies dealing with aeroacoustics. Different model equations can be used to describe the fluctuations. Linearized Euler equations are generally used to predict acoustic wave propagation (see Refs. [17, 39] for recent examples) but do not give any information about the generation of the acoustic waves. Acoustic sources can be modeled using statistical models or evaluated on the basis of normal mode instability waves [49]. In the latter case, the resulting approach can be viewed as a cross between a classical linear stability analysis and CFD techniques. A similar approach is to compute the instability modes associated with the RANS solution, and to identify them with turbulent fluctuations responsible for noise generation. A recent example is the work done by Korrami and Singer [15] in the case of the idealized flow around a flap. A more realistic evaluation of the near-field fluctuations around a mean profile was proposed by Streett [43], who performed a two-dimensional

temporal direct numerical simulation based on the incompressible Navier–Stokes equations. Another technique, referred to as the nonlinear disturbance equations (NLDE) approach, has been developed by Morris and his co-workers to evaluate acoustic sources from a steady jet computation [20–22], on the basis of a nonlinear inviscid model equation for the fluctuations. The second main approximation is that mean flow source terms in the nonlinear disturbance equation can be neglected. More recently, these authors add a subgrid model to the disturbance equations, in order to take into account the effect of unresolved modes. They also did reintroduce a part of the mean flow source term into the nonlinear disturbance equation. The NLDE approach was used by Hansen *et al*. to simulate the unsteady, two-dimensional laminar flow around a circular cylinder [8], corresponding to the first coupling between NLDE with an unsteady mean flow. The first attempt to use it for LES of wall-bounded flow is due to Chyczewski *et al*. [2], who assumed that the fluctuations were incompressible.

The hybrid RANS/LES technique presented in this paper thus appears as the most general case of the NLDE approach, the exact time-dependent signal being split as the sum of an ensemble-averaged part and a remaining fluctuating part, without any additional simplification. Another important feature is the ability of the method to reconstruct the turbulent fluctuations in subdomains embedded in the whole RANS domain, resulting in a significant cost reduction when compared to the classical LES approach, which *a priori* requires computation of an unsteady three-dimensional solution over the whole computational domain.

The present paper first presents a theoretical framework for this hybrid RANS/LES approach, which can be interpreted as a generalized multilevel approach (Section 2) relying on a formal hierarchical decomposition of the exact solution. The associated governing equations for both compressible and incompressible flows are presented in Section 3, and the particular case of the proposed three-level RANS/LES technique is detailed in Section 4. Section 5 presents the results dealing with the assessment of the main features of the method on academic test cases. The proposed method is first shown to be able to predict fully turbulent motion associated with a steady mean flow in the plane channel flow configuration, and its sensitivity to several parameters is discussed. The case of an unsteady mean flow is then analyzed considering a pulsed channel flow. The use of the method to capture the transition to turbulence and fully developed flow around a low-pressure turbine blade is discussed in Section 6. Conclusions and perspectives are given in Section 7.

2. A THEORETICAL MULTILEVEL FRAMEWORK

We first introduce a general theoretical framework for multilevel methods relying on several different scale-separation operators. Let there be a set of restriction operators $\{G_k\}$, $k = 1, N$. The main hypothesis is that these operators have some regularizing properties, in the sense that they render the solution smoother by discarding high frequencies. In the present work, we will focus on RANS/LES approaches, and each operator can be either a spatial filtering operator, as is classically used in LES, or an ensemble average operator, as for the RANS approach.

If the operator G_k corresponds to an ensemble average over the set of samples Ω_k, it is written as

$$G_k(u) \equiv \frac{1}{N_k} \sum_{u_l \in \Omega_k} u_l = \langle u \rangle_{(k)}, \tag{1}$$

where N_k is the number of samples contained in Ω_k. This definition of the ensemble average is valid for both classical mean average and conditional average, depending on the choice of Ω_k. It can represent both steady and unsteady RANS approaches. The ergodic theorem shows that for a statistically stationary field with finite correlation time, this ensemble average can be interpreted as a time-average operator (at least asymptotically).

In the case where a spatial filtering operator is considered, we assume that it can be expressed as a convolution product:

$$G_k(u) \equiv G_k \star u = \int G_k(x-\xi)u(\xi)\,d\xi. \tag{2}$$

This expression of the convolution filter is very general, and the problem of its extension to bounded domains and/or curvilinear meshes is still a research topic. Second-order-accurate extensions for bounded domains and curvilinear meshes were proposed by Ghosal and Moin [7] and generalized to arbitrary order of accuracy by Vasyliev *et al.* [48]. Time-filtering operators have recently been studied by Pruett [27].

It is important to note that the developments presented below are fully general and can be applied to all the ensemble average/filtering operators.

Using this family of operators, we can define a set of hierarchical scale-separation operators $\{\mathcal{G}_1^k\}$, $k=1, N$:

$$\mathcal{G}_1^k = G_k \circ G_{k-1} \circ \cdots \circ G_1 = G_k \circ \mathcal{G}_1^{k-1}. \tag{3}$$

A set of hierarchical regularized representations of the field u, $\{\bar{u}^k\}$, $k=\{1,\ldots,N\}$, can then be defined as

$$\bar{u}^k \equiv \mathcal{G}_1^k(u). \tag{4}$$

The kth-level fluctuation v_k is defined as

$$v_k \equiv u - \bar{u}^k = \left(I_d - \mathcal{G}_1^k\right)(u), \tag{5}$$

where I_d is the identity operator.

By analogy with the classical multiresolution framework as developed by Harten [9] the details $w_{k,l}$, $l>k$, defined as the difference between the two levels of resolution l and k, are evaluated as follows:

$$w_{k,l} \equiv \bar{u}^k - \bar{u}^l = (I_d - G_l \circ \cdots \circ G_{k+1}) \circ \mathcal{G}_1^k(u). \tag{6}$$

Completing the filter family by setting $G_0 = Id$, we obtain $w_{k,0} = v_k$.

Relation (6) yields the following multilevel decomposition of the data:

$$u = \bar{u}^k + \sum_{l=1,k} w_{l,l-1}, \quad \forall k \in [1, N]. \tag{7}$$

Using Eqs. (5) and (7), we can rewrite the fluctuation v_k as a function of the details:

$$v_k = \sum_{l=1,k} w_{l,l-1}, \quad \forall k \in [1, N]. \tag{8}$$

This multilevel decomposition is an extension of the one proposed by Terracol and coworkers [34, 45, 46], who developed a similar decomposition in the restricted case of multilevel LES algorithms. The main difference is that, in the present case, the hierarchical scale-separation operators $\mathcal{G}_1^k$ can be hybrid ensemble average/convolution filter operators. If each scale-separation operator can be associated with a particular cutoff frequency, the proposed decomposition can also be interpreted as a more general expression of the multiresolution decomposition of the data, as proposed by Harten [9]. This is especially true for convolution filters based on hierarchical operators, which lead to the definition of multilevel LES algorithms. A similar formal decomposition was used by Quéméré and coworkers [28, 29, 34] to derive zonal hybrid RANS/LES and zonal multiresolution LES/LES techniques.

Other mixed scale-separation procedures have been proposed by several authors: Yoshizawa makes use of a combined statistical average/truncated Fourier expansion decomposition, while Germano proposes a more general multiscale LES decomposition and a hybrid statistical average/filtering operator in order to derive hybrid RANS/LES models. Most of these previous works are summarized in Ref. [6].

3. MATHEMATICAL MODEL

3.1. General Formulation

We consider the case of Newtonian compressible or incompressible fluids described by the Navier–Stokes equations. Let U be the vector corresponding to the exact solution of these equations, which are written in compact form as

$$NS(U) = 0 = \frac{\partial U}{\partial t} + \nabla \cdot F(U), \tag{9}$$

where NS is the Navier–Stokes operator. Operator F represents the fluxes, which are nonlinear functions of U.

We now introduce the commutator $[.,.]$ of two operators, a and b:

$$[a, b](U) = a \circ b(U) - b \circ a(U). \tag{10}$$

It has the following properties:

$$[\mathcal{F}, \mathcal{G}] = -[\mathcal{G}, \mathcal{F}], \text{ skew symmetry;} \tag{11}$$

$$[\mathcal{F} \circ \mathcal{G}, \mathcal{H}] = [\mathcal{F}, \mathcal{H}] \circ \mathcal{G} + \mathcal{F} \circ [\mathcal{G}, \mathcal{H}], \text{ Germano's identity;} \tag{12}$$

$$[\mathcal{F}, [\mathcal{G}, \mathcal{H}]] + [\mathcal{G}, [\mathcal{H}, \mathcal{F}]] + [\mathcal{H}, [\mathcal{F}, \mathcal{G}]] = 0, \text{ Jacobi's identity.} \tag{13}$$

Applying the scale-separation operator $\mathcal{G}_1^k$ to Eq. (9), we get the governing equations for the kth-level filtered variable $\bar{u}^k$:

$$NS(\bar{U}^k) = \frac{\partial \bar{U}^k}{\partial t} + \nabla \cdot F(\bar{U}^k) = -\left[\mathcal{G}_1^k, NS\right](U) = -\tau^k. \tag{14}$$

The term on the right-hand side accounts for all the commutation errors which arise when the scale-separation operator is applied to the Navier–Stokes equations, including commutation errors associated with a possible anisotropy of the filter, boundary conditions, and even numerical errors when discretized equations are considered.

In the simplest case, where the scale-separation operator commutes with all space and time derivatives, the commutation error simplifies in classical RANS and LES expressions, corresponding to the force exerted by unresolved modes on the resolved ones:

$$\tau^k = \left[\mathcal{G}_1^k, NS\right](U) = \left[\mathcal{G}_1^k, \nabla \cdot F\right](U) = \nabla \cdot \left[\mathcal{G}_1^k, F\right](U). \tag{15}$$

The only source of commutation errors are the nonlinearities of the Navier–Stokes equations, which appear in the convection term and possibly in the viscous terms when temperature-dependent viscosity and diffusivity are considered. The force τ^k is classically written as the divergence of the Reynolds or subgrid stresses, $\mathcal{T}^k$, for RANS and LES, respectively, which must be modeled (i.e., expressed as a function of $\bar{U}^k$) in order to get a closed problem. The closure can be written symbolically as

$$\tau^k = \left[\mathcal{G}_1^k, NS\right](U) = \nabla \cdot \mathcal{T}^k \approx \mathcal{M}(\bar{U}^k), \tag{16}$$

where $\mathcal{M}(\bar{U}^k)$ is a statistical model.

The evolution equations for the details are obtained using Eqs. (14) and (6):

$$\frac{\partial w_{k,l}}{\partial t} + \nabla \cdot F(\bar{U}^k) - \nabla \cdot F(\bar{U}^l) = \tau^l - \tau^k. \tag{17}$$

3.2. Compressible Flow Model

We now present explicitly the governing equations for compressible flows. The solution vector is $U = (\rho, \rho V^T, E)^T$, where ρ is the density, $V = (u, v, w)^T$ the velocity, and E the total energy.

The fluxes are expressed as

$$F(U) = \begin{pmatrix} \rho V \\ \rho V \otimes V + pId - \sigma \\ (E + p)V - \sigma : V + Q \end{pmatrix}, \tag{18}$$

where p is the pressure and Id the identity tensor. The viscous stress tensor σ is given by the law

$$\sigma = 2\mu(T)\left(S - \frac{1}{3}tr(S)Id\right), \tag{19}$$

where $S = \frac{1}{2}(\nabla V + \nabla^T V)$ and $\mu(T)$ is the dynamic viscosity computed following Sutherland's law.

The temperature T is given by the perfect-gas-state law,

$$p = R\rho T, \tag{20}$$

with R the perfect gas constant. The viscous heat flux vector Q is given by

$$Q = -\kappa(T)\nabla T, \tag{21}$$

where $\kappa(T)$ is the diffusivity, which can also be computed as a function of T using Sutherland's law.

The kth-level filtered vector is $\bar{U}^k = (\bar{\rho}^k, (\overline{\rho V}^k)T, \bar{E}^k$. With the introduction of Favre's change of variables based on a mass weighting, it can also be written $\bar{U}^k = (\bar{\rho}^k, (\bar{\rho}^k \tilde{V}^k)^T, \bar{E}^k)$.

The total energy being a nonlinear function of pressure, density, and velocity, i.e., $E = E(\rho, p, V)$, the term $\tilde{E}^k$ will introduce new commutation error terms. To simplify these terms, it is possible, following Vreman [50], to define the resolved total energy at level k as $\hat{E}^k = E(\bar{\rho}^k, \bar{p}^k, \tilde{V}^k)$, leading to $\bar{U}^k = (\bar{\rho}^k, (\bar{\rho}^k \tilde{V}^k)^T, \hat{E}^k)$. Resolved viscous stresses and heat fluxes are defined in the same way,

$$\hat{\sigma}^k = 2\bar{\mu}^k(\bar{T}^k)\left(\tilde{S}^k - \frac{1}{3}tr(\tilde{S}^k)Id\right) \neq \bar{\sigma}^k, \tag{22}$$

with $\tilde{S}^k \equiv \frac{1}{2}(\nabla \tilde{V}^k + \nabla^T \tilde{V}^k)$ and

$$\hat{Q}^k = -\bar{\kappa}^k(\bar{T}^k)\nabla \bar{T}^k \neq \bar{Q}^k. \tag{23}$$

Using this form of the kth-level solution, we get the following form of the commutation error in the simple case where derivatives and scale-separation operators commute:

$$\tau^k = \nabla \cdot \begin{pmatrix} 0 \\ (\bar{\rho}^k V \widetilde{\otimes} V^k - \bar{\rho}^k \tilde{V}^k \otimes \tilde{V}^k) - (\bar{\sigma}^k - \hat{\sigma}^k) \\ (\overline{(E+p)V}^k - (\hat{E}^k + \bar{p}^k)\tilde{V}^k) - (\overline{\sigma : V}^k - \hat{\sigma}^k : \tilde{V}^k) + (\bar{Q}^k - \hat{Q}^k) \end{pmatrix}. \tag{24}$$

The use of the new definition of the resolved total energy makes also the additional term $\frac{\partial}{\partial t}(\bar{E}^k - \hat{E}^k)$ appear in the energy equation, but this term is usually neglected or added to the pressure term.

3.3. Incompressible Flow Model

We now describe the governing equation for an incompressible flow using a velocity–pressure formulation. The solution vector is $U = V = (u, v, w)^T$, and the fluxes are expressed as

$$F(U) = V \otimes V + pId - \nu(\nabla V + \nabla^T V), \tag{25}$$

where p and ν denote the static pressure and the kinematic viscosity, respectively. The incompressibility constraint yields

$$\nabla \cdot V = 0. \tag{26}$$

The associated filtered relation at the kth level is

$$\nabla \cdot \bar{V}^k = -\left[\mathcal{G}_1^k, \nabla \cdot\right](V). \tag{27}$$

In the same way, the continuity equation associated with the detail $w_{k,l}$ is

$$\nabla \cdot w_{k,l} = \left[\mathcal{G}_1^l, \nabla \cdot\right](V) - \left[\mathcal{G}_1^k, \nabla \cdot\right](V). \tag{28}$$

It is worth noting that the two filtered continuity equations, (27) and (28), show that neither the filtered variables nor the details are solenoidal if the scale-separation operators do not commute with the divergence operator.

Assuming that the derivatives and scale-separation operators do commute, we get

$$\tau^k = \nabla \cdot (\overline{V \otimes V}^k - \bar{V}^k \otimes \bar{V}^k). \tag{29}$$

In the computation presented below, the scale-separation operators were chosen such that they commute with space and time derivatives, yielding the definition of solenoidal resolved field and details.

4. APPLICATION TO RANS/LES COUPLING

The hybrid RANS/LES approach proposed here relies on the definition of three components of the solution: the mean flow, the resolved fluctuating flow, and the unresolved fluctuating flow. It is then associated with a three-level decomposition, based on two different operators, G_1 and G_2, which are of different nature. The first operator, G_1, is a classical LES filtering operator, while G_2 is a Reynolds ensemble average operator.

In order to render the notations as clear as possible, the ensemble average operator will be noted using brackets (the simplified notation $\langle\,\rangle$ is used instead of $\langle\,\rangle_{(1)}$ because only one ensemble average operator is involved), and the convolution filter will be noted using a bar, yielding

$$\bar{U}^2 = \langle \bar{U} \rangle, \quad \bar{U}^1 = \bar{U}. \tag{30}$$

The resulting decomposition is

$$U(x,t) = \underbrace{\bar{U}^2}_{\langle \bar{U} \rangle} + \underbrace{w_{1,2}}_{\bar{U} - \langle \bar{U} \rangle} + \underbrace{w_{0,1}}_{U - \bar{U}}, \tag{31}$$

where the details $w_{1,2}$ are the resolved fluctuations around $\langle \bar{U} \rangle$ and $w_{0,1}$ is the unresolved fluctuations, which will be modeled using an usual subgrid model.

The strategy proposed here to compute the field is to use a classical method based on Eq. (14) to obtain the RANS field $\langle \bar{U} \rangle$, and then to use a LES method based on Eq. (17) to compute the details $w_{1,2}$. The key point of the method consists of solving equations for $w_{1,2}$ only, and not for the whole field $\bar{U}^1$, as was the case for multilevel LES algorithms [4, 45, 46].

It is worth noting that the resulting algorithm leads to a one-way coupling: LES retrieves some information from the RANS computation (sources and cross terms in Eq. (17)), but no feedback from LES to RANS is present. Such a feedback could be obtained by computing the turbulent force from LES and substituting the parametrized source term τ^2 into the RANS equations and repeating this procedure. This procedure, which requires a large amount of CPU time, was not implemented during the present study.

An interesting point is that, in the present approach, due to the definition of a hierarchical set of scale-separation operators, the ensemble average of the filtered solution $\langle \bar{U} \rangle$ appears at the last level, while the ensemble- averaged exact solution $\langle U \rangle$ is used if a classical RANS

equation is solved to compute the mean field. These two decompositions are equivalent if $\langle \bar{U} \rangle = \langle U \rangle$, i.e., if the filter does not modify the ensemble-averaged flow. This is the case when the filter is restricted to homogeneous direction of the flow with constant grid spacing. When filtering is applied in inhomogeneous directions, or when inhomogeneous filters are considered, these two quantities can differ, at least from a theoretical point of view [38].

Depending on the turbulence model used at each level, the corresponding pressure can be replaced by the pseudopressure p^*, which is defined as the sum of the pressure at the considered level and the turbulent kinetic energy. Thanks to the fact that no feedback from $w_{1,2}$ is taken into account in the equation for $\langle \bar{U} \rangle$, the turbulent force $-\tau^2$ can be parametrized using a classical RANS turbulence model. But it is worth noting that the whole field $\bar{U}^1 = \langle \bar{U} \rangle + w_{1,2}$ is required to compute τ^1 with usual subgrid models.

In the present study, eddy–viscosity-type models are used both at the RANS and the LES level. The unresolved force term τ^i is computed as

$$\tau^i = -\nabla \cdot (\mu_i \cdot (\nabla \bar{V}^i + \nabla^T \bar{V}^i)), \tag{32}$$

where the eddy–viscosity μ_i is computed using a model. In the present study, classical closures have been used at each level, which are be discussed in the present paper: the Jones–Launder $k - \varepsilon$ model [14] and the Spalart–Allmaras model [40] for RANS equations and the selective mixed scale model [33, 35] for the LES equations. The models are described in the Appendices.

5. ASSESSMENT OF THE METHOD ON ACADEMIC TEST CASES

This section is devoted to the assessment of the method on basic test cases, which correspond to incompressible flows. The numerical method is discussed in Section 5.1.

Results are presented in sections below. First, in Section 5.3, the ability of the method to reconstruct unsteady fluctuations associated with developed turbulence around a steady mean velocity profile is assessed on a plane channel flow. The robustness of the method with respect to the size of the computational domain, the grid resolution, and the error commited on the mean flow $\langle \bar{U} \rangle$ is investigated. Then, the case of an unsteady mean velocity profile is considered in Section 5.4, in order to validate the general character of the proposed hybrid approach. The selected configuration is the periodically pulsed plane channel flow. For this flow, the unsteadiness of the ensemble-averaged flow can be directly related to the notion of phase average locked on the pulsation period.

In all theses cases, the mean flow field $\langle \bar{U} \rangle$ is associated with a 1D (one space dimension, steady case) or a 2D (one space and one time dimension, pulsed case) problem, while the computation of the turbulent fluctuations is based on a 4D simulation (three space and one time dimension).

5.1. Numerical Method

The LES numerical method is the same as in Ref. [35]. It is based on a centered second-order-accurate discretization for the spatial derivatives. This implies that no artificial dissipation is introduced by the numerical scheme. In order to minimize the aliasing errors, the convection term is written in skew–symmetric form. Time integration is performed using a semi-implicit integration procedure. Viscous terms are integrated using a

second-order-accurate backward Euler scheme, while convection terms are treated using an explicit second-order Adams–Bashforth scheme. Subgrid terms are split in order to separate dispersive and diffusive contributions. Diffusive contributions are integrated in the same way as the viscous terms, while the dispersive ones are treated like the convection terms. Linear systems are solved using a BiCGSTAB method, peconditioned by the inverse of the diagonal.

For classical LES computations, a forcing term identical to the one used in Ref. [35] is employed to enforce a constant mass flow rate.

The simulations are initialized by a randomized, divergence-free field.

5.2. Computational Parameters

All the computations are related to the biperiodic plane channel flow. The mean flow direction, the wall-normal direction, and the spanwise direction are x, z, and y, respectively. A Cartesian grid is employed. For the LES computations, a uniform grid spacing is used in the homogeneous direction (x and y), while a hyperbolic stretching is applied to the wall-normal direction. A one-dimensional stretched grid with the same node distribution as for the LES grid is used for the computation of the one-dimensional statistical field.

The mean value of the friction Reynolds number $Re_\tau = hu_\tau/\nu$, where h is the channel half-height and u_τ the friction velocity, is taken equal to 395 for all the computations presented in this paper.

Several combinations of domain size and grid resolution for the computation of the fluctuations were investigated in order to compare both the robustness and the accuracy of the hybrid method with those of the classical LES approach. All the cases are summarized in Table I.

Four domain sizes were considered.

1. A classical domain for LES-type simulation (cases Dom1, Dom2, Dom3, and Dom4). In order to prevent spurious coupling of the fluctuations in homogeneous directions, the domain size in the x and y direction, L_x and L_y, respectively, has been chosen such that $L_x^+ \approx 5000$, $L_y^+ \approx 1200$, where superscript $+$ is related to wall units. The height of the channel $L_z = 2h$ corresponds to $L_z^+ = 790$, corresponding to a full channel configuration.

2. A half-channel configuration, which has the same characteristics as the previous case in the x and y directions, but only one solid wall is taken into account, and an arbitrary symmetry boundary condition is imposed at the centerline of the channel (case Dom5). This case is known to be a very difficult one for classical LES, because of the random unsteady

TABLE I
Geometrical Parameters for Channel Computations

Case	L_x^+	L_y^+	L_z^+	N_x	N_y	N_z	Δx^+	Δy^+	Min (Δz^+)
Dom1	4964	1240	790	64	64	67	78	18	1
Dom2	5192	1188	790	44	44	67	118	27	1
Dom3	4964	1240	790	64	64	23	78	18	4.8
Dom4	4964	1240	790	64	64	19	78	18	10
Dom5	4964	1240	395	64	64	34	78	18	1
Dom6	468	108	790	6	6	67	78	18	1
Dom7	468	108	395	6	6	34	78	18	1

behavior of the field which is not consistent with usual boundary conditions (see the works of Jimenez and Vasco [13] on the half-channel flow problem and those of Nicoud *et al.* [24]).

3. A minimal channel unit domain [10], with $L_x^+ = 468$, $L_y^+ = 108$ (case Dom6). This domain size is close to those used by Jimenez and Pinelli [11]. The purpose here is to see how much the domain size can be reduced while keeping a reliable description of the autonomous cycle of near-wall turbulence with a relatively coarse grid, and how the hybrid procedure compares with classical LES. The present domain size is compatible with recent investigations dealing with the low-dimensional dynamics of turbulent wall flows [10–12, 51]. Following the idea of Jimenez and Simens [12], this "minimal cell" could be used in practical cases by defining a "crystal" of identical cells in regions where the mean flow is homogeneous or slowly varying. This strategy has been implemented by Pascarelli and Piomelli on a turbulent boundary layer configuration [25].

4. A half-minimal channel unit (case Dom7): the same as above, but with a truncated domain in the wall-normal direction. It is worth noting that the present computations correspond to a true half-domain computation, while a filter was imposed on a full-domain computation in Refs. [11, 12]. The wall-normal dimension is taken equal to 395 wall units, which is higher than the minimum value of 60–70 wall units given by Jimenez and his co-workers and is also compatible with the size of "exact" coherent structures as defined by Waleffe [51].

Different grid resolutions were selected.

1. A "medium-resolution grid," with $\Delta x^+ = 78$ and $\Delta y^+ = 18$ (cases Dom1, Dom5, Dom6, Dom7). The stretching in the wall-normal direction is made in order to obtain $\Delta z^+ = 1$ for the first grid point near the wall. This grid resolution, used together with a second-order-accurate method, is expected to yield reliable results for classical LES [52, 53].

2. A "coarse-resolution grid," with $\Delta x^+ = 118$ and $\Delta y^+ = 27$, on which classical LES based on a second-order-accurate method is expected to yield bad results [52, 53] (case Dom2).

3. A coarsened medium grid in the wall-normal direction, in order to investigate the ability of the hybrid computation to capture turbulence production on badly resolved mesh. The first grid point near the wall is located at $\Delta z^+ = 4.8$ and 10 in cases Dom3 and Dom4, respectively.

Statistical moments of the fluctuations are computed by collecting samples in time and in homogeneous directions. It was checked that the sampling was sufficient to ensure the convergence of the presented results.

5.3. Statistically Steady Plane Channel Flow

Several mean flow profiles were used for the computation of the fluctuations using the hybrid RANS/LES method, in order to analyze the sensitivity of the results on the error commited on the mean flow. These are as follows:

1. Computation of the mean flow by carrying out a RANS computation. In the present case, the Jones–Launder $k - \varepsilon$ model [14] was used. A one-dimensional simulation was performed. The numerical procedure was based on the compressible Navier–Stokes equations, but the Mach number was kept low enough to prevent any compressibility effects. The numerical method is based on a finite-volume cell-centered approach, using the Jameson

numerical scheme. Steady solution was obtained using a time-marching procedure based on an explicit time integration (four-step Runge–Kutta scheme) with implicit residual smoothing. The convergence rate was improved using a local time stepping. The fluctuating field being computed using a finite-difference method, the computed mean velocity is linearly interpolated at the grid nodes.

2. Computation of the mean flow by performing an ensemble average of a LES computation. In the present computation, mean flow of the A1 case (classical LES on Dom1) was selected. Fluctuations reconstructed using this definition of the mean flow are expected to exhibit the smallest discrepancies with the classical LES results.

3. Making use of an analytical profile of the mean velocity profile. Assuming the symmetry of the profile with respect to the channel centerline, we have, for one-half of the channel,

$$u^+(z^+) = \begin{cases} z^+, & \text{if } z^+ < 11.83, \\ \frac{1}{0.4}\log(z^+) + 5.5, & \text{otherwise.} \end{cases} \tag{33}$$

It is interesting to note that the resulting profile is singular at the centerline at the channel, since its gradient is discontinuous.

4. Selecting a uniform mean flow which corresponded to the inviscid solution. This case presents the maximum discrepancy with the real mean velocity profile.

These four prescribed mean velocity profiles are displayed in Fig. 1. All the computational cases are summarized in Table II. The first line corresponds to classical LES computations. The last four lines correspond to hybrid computations, with different evaluations of the mean flow $\langle \bar{U} \rangle$: "$k - \varepsilon$" is related to the use of steady RANS computation results, $\langle LES \rangle$ refers to the use of mean flow computed from LES on Dom1, and *analytical* and *Euler* correspond to the use of the analytical profile and the uniform flow, respectively. The dash denotes cases which were not considered, and the check mark is related to computations which were unable to sustain a stable turbulent flow.

An important point of the method deals with the practical computation of the turbulent RANS fluxes, which appear in the right-hand side of the LES-type equations for the details (term τ^l in Eq. (17)). Numerical experiments show that numerical instability occurs when the imposed mean flow is assumed to be statistically steady and that the imposed discrete mean field does not correspond to a fully converged solution with the numerical method employed to solve the equations for the fluctuations, i.e., when $\partial \langle \bar{U} \rangle / \partial t \neq 0$ from a discrete point of view. This is the case when the mean flow is not computed with the same numerical method on the same grid as the fluctuations with complete convergence. This difference corresponds to the introduction of a spurious forcing term in the equations for the fluctuations. A simple way to alleviate this problem consists of recomputing explicitly the turbulent term τ^2 using the field $\langle \bar{U} \rangle$ on the same mesh as used for the fluctuations with the same numerical method rather than using the value predicted by the turbulence model, yielding

$$-\tau^2 = \nabla \cdot (\langle \bar{V} \rangle \otimes \langle \bar{V} \rangle + \langle \bar{p} \rangle Id - \nu(\nabla \langle \bar{V} \rangle + \nabla^T \langle \bar{V} \rangle)). \tag{34}$$

This new way to compute the turbulent force makes it possible to generate equilibrium solutions no matter which solution was used to define the prescribed velocity field.

The results obtained with the proposed approach are compared with a classical LES computation on the finest grid considered in this paper and the largest computational domain (case A1). This LES computation has been previously discussed in Ref. [35].

TABLE II
List of Steady Channel Computations

	Case						
	Dom1	Dom2	Dom3	Dom4	Dom5	Dom6	Dom7
Classical LES	A1	A2	√	√	√	√	√
$k-\varepsilon$	B1	B5	B9	B11	—	B15	B18
$\langle LES \rangle$	B2	B6	B10	B12	B13	B16	B19
Analytic	B3	B7	—	—	B14	B17	B20
Euler	B4	B8	—	—	—	—	—

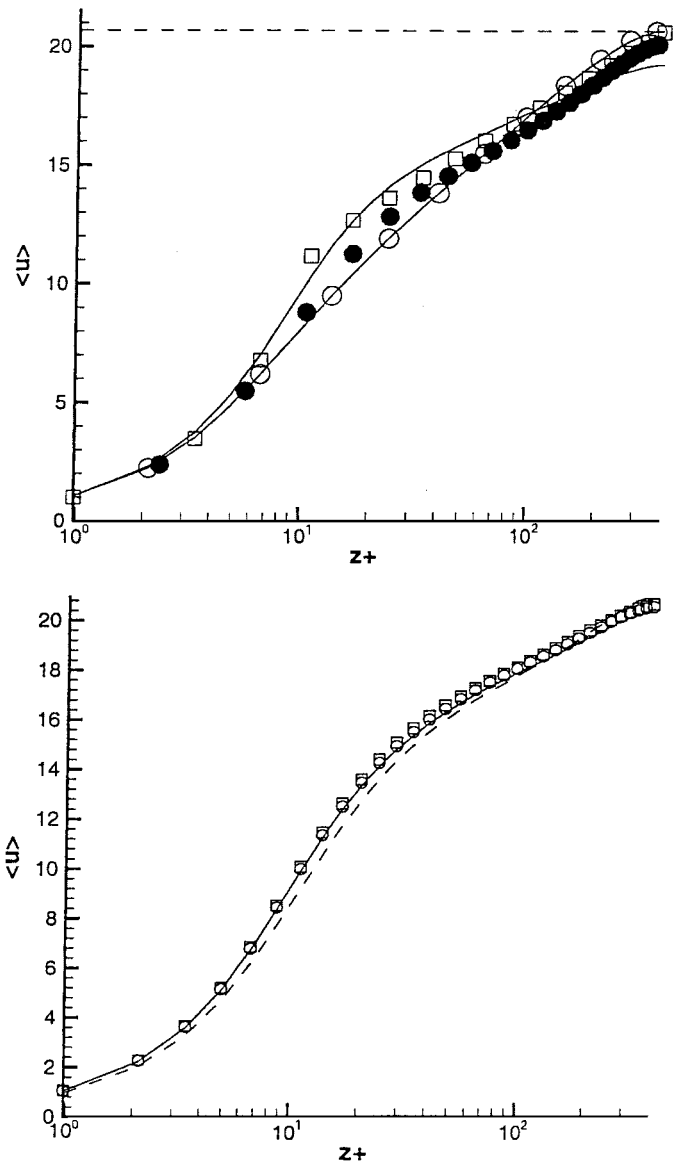

FIG. 1. Stationary channel computation. Prescribed $\langle \bar{V} \rangle$ (top) and corrected $\langle \bar{V} \rangle + \langle w_{1,2} \rangle$ (bottom) mean velocity profile. ●, DNS mean velocity field; solid line, classical LES mean velocity field; ⊖, D1 case; □, D2 case; dashed line, D3 case.

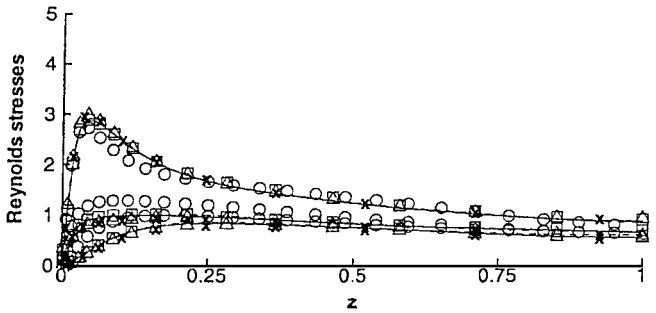

FIG. 2. Stationary channel computation, resolved Reynolds stresses. Circles, DNS (Moser *et al*. [23]); solid line, LES (case A1); dashed line, hybrid (case B2); triangles, hybrid (case B3); crosses, hybrid (case B4); squares, hybrid (case B1).

The total corrected mean velocity profile, defined as the sum of the prescribed mean flow and the averaged fluctuating field, is shown in Fig. 1. The ability of the hybrid method to alleviate problems in the definition of the prescribed mean flow is clearly observed. Computed resolved Reynolds stresses computed *with respect to the total corrected mean flow* on the full channel configuration with the medium and the coarse meshes are displayed in Figs. 2 to 5. On the fine mesh, all the hybrid computations yield nearly identical results, in very good agreement with classical LES on the same mesh. This lack of sensitivity to the prescribed mean velocity field is explained by the fact that all the inconsistencies between the mean velocity field and the governing equations for the fluctuations will be removed during the integration by the growth of a nonzero mean fluctuating field. This point is clarified by combining Eqs. (17) and (31). The resulting evolution for the mean value of the fluctuating field is obtained:

$$\frac{\partial \langle w_{1,2} \rangle}{\partial t} = -\langle \nabla \cdot F(\bar{U}^1) - \nabla \cdot F(\bar{U}^2) \rangle + \langle \tau^2 - \tau^1 \rangle \tag{35}$$

$$= 0. \tag{36}$$

Relation (36) holds for the ideal continuous equation only: numerical and modeling errors result in a nonzero right-hand side in Eq. (35) and thus to a nonzero value *of* $\langle w_{1,2} \rangle$.

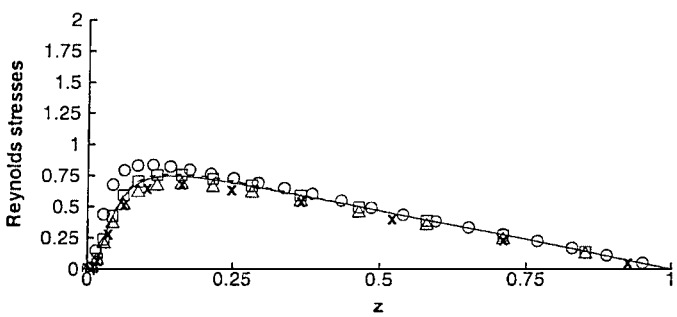

FIG. 3. Stationary channel computation, resolved shear stress. Circles, DNS (Moser *et al*. [23]); solid line, LES (case A1); dashed line, hybrid (case B2); triangles, hybrid (case B3); crosses, hybrid (case B4); squares, hybrid (case B1).

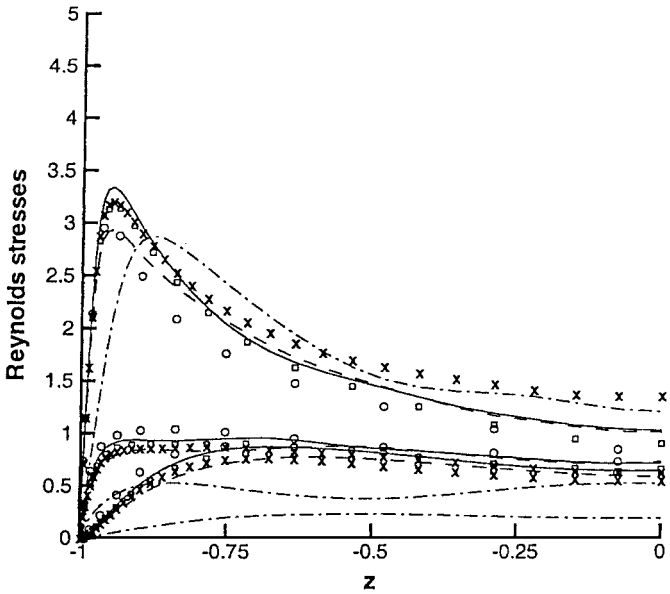

FIG. 4. Stationary channel computation, resolved Reynolds stresses. Circles, LES (case A1); dash–dots, LES (case A2); solid line, hybrid (case B6); dashed line, hybrid (case B5); crosses, hybrid (case B8); squares, hybrid (case B7).

Numerical errors include both discretization errors, incomplete convergence in the computation of the mean flow, or possible interpolation errors if different grids are used to compute the mean and fluctuating fields. As a consequence, Reynolds stresses computed using the hybrif procedure must be defined with respect to the corrected mean flow field $\bar{U}^2 + \langle w_{1,2} \rangle$.

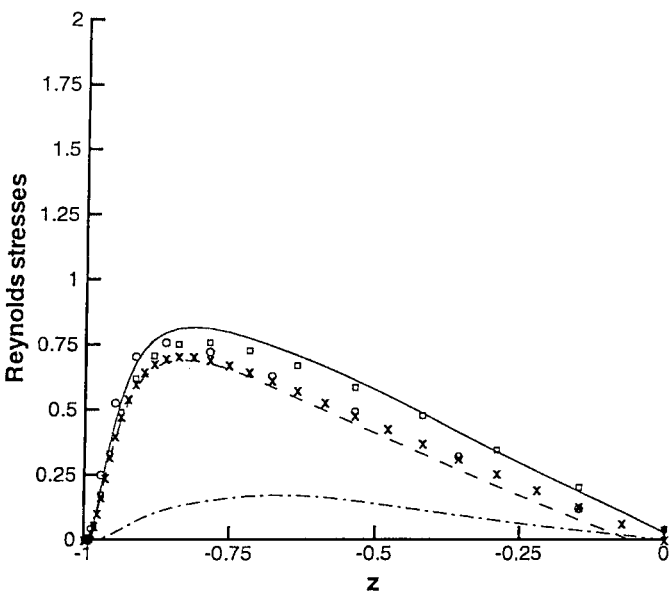

FIG. 5. Stationary channel computation, resolved shear stress. Circles, LES (case A1); dash–dots, LES (case A2); solid line, hybrid (case B6); dashed line, hybrid (case B5); crosses, hybrid (case B8); squares, hybrid (case B7).

Another source for nonzero values of $\langle w_{1,2} \rangle$ is the possible difference between $\langle \bar{U} \rangle$ and $\langle U \rangle$ (see discussion in Section 4): relation (31) then leads to

$$\langle w_{1,2} \rangle = \langle \bar{U} \rangle - \langle U \rangle, \tag{37}$$

showing that the fluctuating will adapt itself to correct some filtering effects on the mean flow in nonhomogeneous directions.

On the coarse mesh, the use of the hybrid approach is seen to yield much better results than the classical LES on the same grid, compared with the results of the LES on the fine grid. The coarse-grid LES exhibits lower peak values of the Reynolds stresses, and maxima are moved toward the center of the channel. These observations are in agreement with previous observations of many authors. This improvement is observed for all the prescribed mean velocity fields, but the best results are obtained when a mean LES velocity field is prescribed. NLDE results dealing with an incompressible turbulent flat-plate boundary layer were presented in Ref. [2] with a coarser mesh ($\Delta x^+ = 184$, $\Delta y^+ = 48$). These results exhibit the same trends as the present LES on the coarse mesh (peaks are flattened and moved toward the center of the channel). That shows that a too-coarse grid resolution for hybrid RANS/LES computations may result in loss of accuracy of the method. The fact that the differences observed when different mean velocity fields are used are larger than on the fine grid shows that the ability of the method to remove the inconsistencies between the precribed mean velocity field and the fluctuation is directly governed by the grid resolution. Consequently, $\Delta x^+ = 120$ and $\Delta y^+ = 30$ seem to be maximum recommended values for a good description of near-wall turbulence using the hybrid approach.

Results obtained using the coarsened grid in the wall-normal direction are shown in Figs. 6 and 7. A very good agreement with classical LES with the usual ($\Delta z^+ = 1$) grid resolution is recovered in case Dom3 ($\Delta z^+ \approx 5$) for all the considered prescribed mean velocity fields, while case Dom4 ($\Delta z^+ = 10$) is too coarse to permit a reliable description of the near-wall dynamics. It is important to note that classical LES on these coarsened grids was not able to sustain a stable turbulent solution. A much coarser grid was used in Ref. [2] ($\Delta x^+ = 250$, $\Delta y^+ = 32$, $\Delta z^+ = 25$) with and without wall models, yielding poor

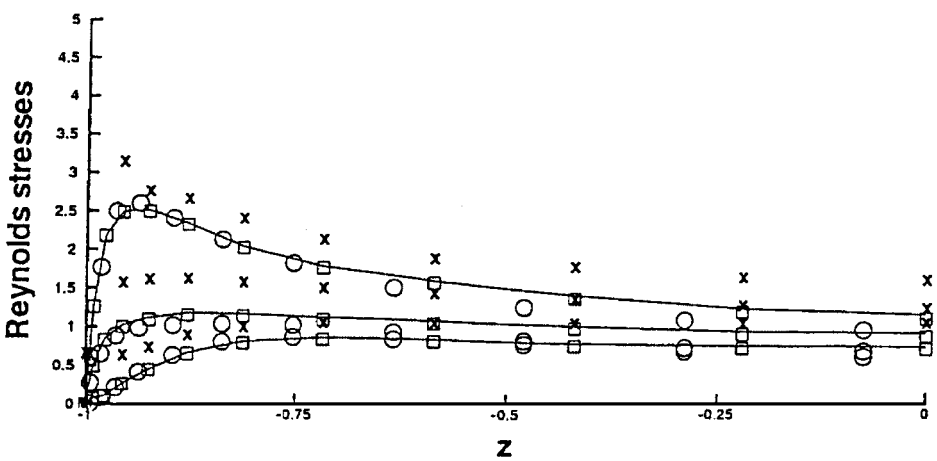

FIG. 6. Stationary channel computation, resolved Reynolds stresses. Circles, LES (case A1); solid line, hybrid (case B10); crosses, hybrid (case B12); squares, hybrid (case B9).

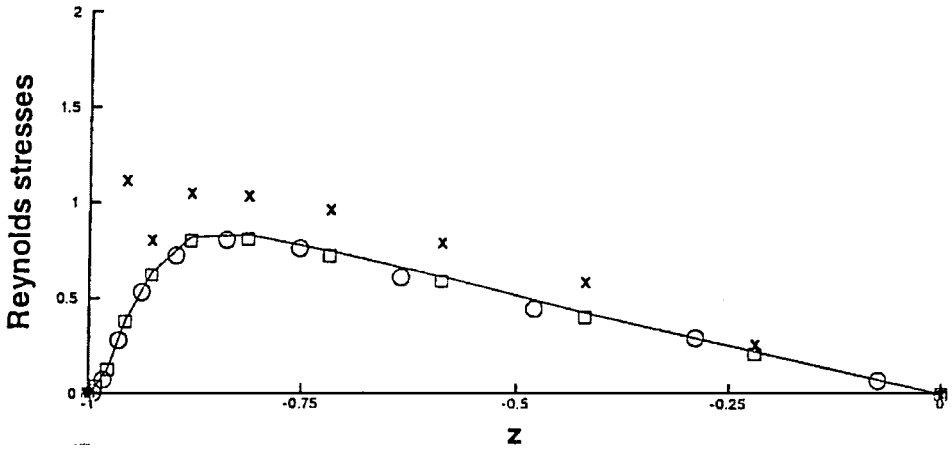

FIG. 7. Stationary channel computation, resolved shear stress. Circles, LES (case A1); solid line, hybrid (case B10); crosses, hybrid (case B12); squares, hybrid (case B9).

results. This indicates that $\Delta z^+ \approx 5$ appears to be a maximum for the first mesh near the wall, at least if efficient wall models are not employed.

Results corresponding to the minimal channel configuration are shown in Figs. 8 and 9. The first point to note is that classical LES was not able to sustain stable turbulent solutions with the present resolution. It is worth recalling here that spectral methods were used in Refs. [10–12] with a much finer resolution ($\Delta x^+ < 15$, $\Delta y^+ \leq 8$) to get DNS results on the minimal channel configuration. The quality of the present results is satisfactory and compares well with the one presented in Ref. [11] and the classical LES on the full channel configuration, no matter which prescribed mean velocity field is employed. Once again, the best results are obtained when the mean LES velocity field is used.

Finally, results dealing with the half-channel configuration are plotted in Figs. 10 and 11. The hybrid method yields satisfactory results on the full channel configuration, while larger discrepancies are observed on the minimal channel configuration. It is worth recalling that

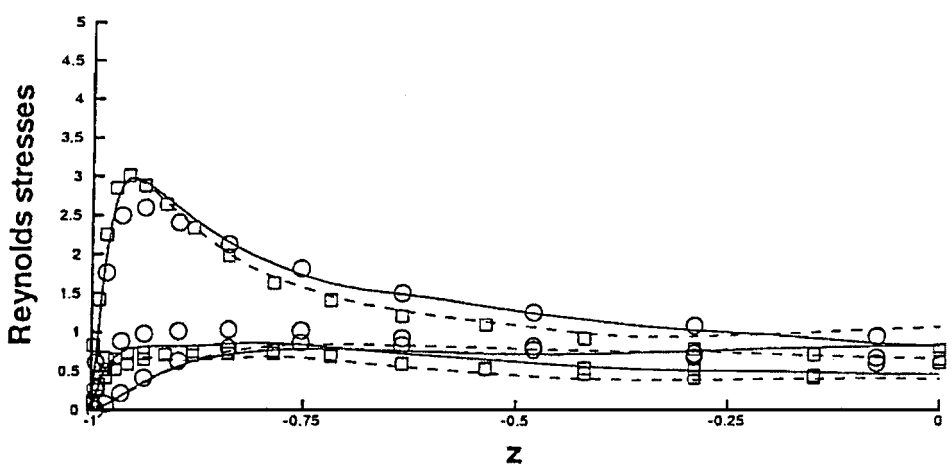

FIG. 8. Stationary channel computation, resolved Reynolds stresses. Circles, LES (case A1); solid line, hybrid (case B16); dashed line, hybrid (case B17); squares, hybrid (case B15).

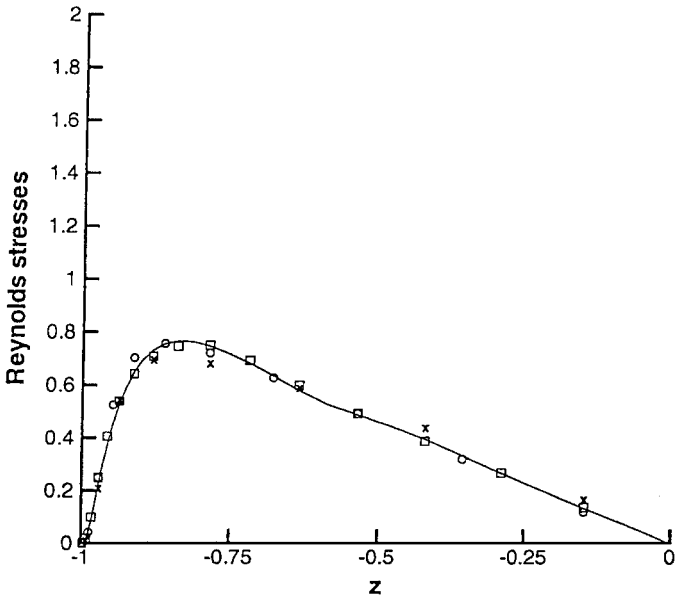

FIG. 9. Stationary channel computation, resolved shear stress. Circles, LES (case A1); solid line, hybrid (case B16); dashed line, hybrid (case B17); squares, hybrid (case B15).

a symmetry condition is imposed at the channel centerline in all the computations. The classical LES do not lead to stable turbulent results, while all the hybrid computations yield reliable results. This can be explained by the fact that the error is commited on the fluctuating field only, the mean field being not affected. An interesting feature of the hybrid RANS/LES method is that the error seems to remain located in a small region (four to five grid point wide) near the artificial symmetry plane. It is worth nothing that previous work [13, 24] dealing with the half-channel configuration yield poor results or make use of very complex boundary conditions on the artificial boundary at the channel

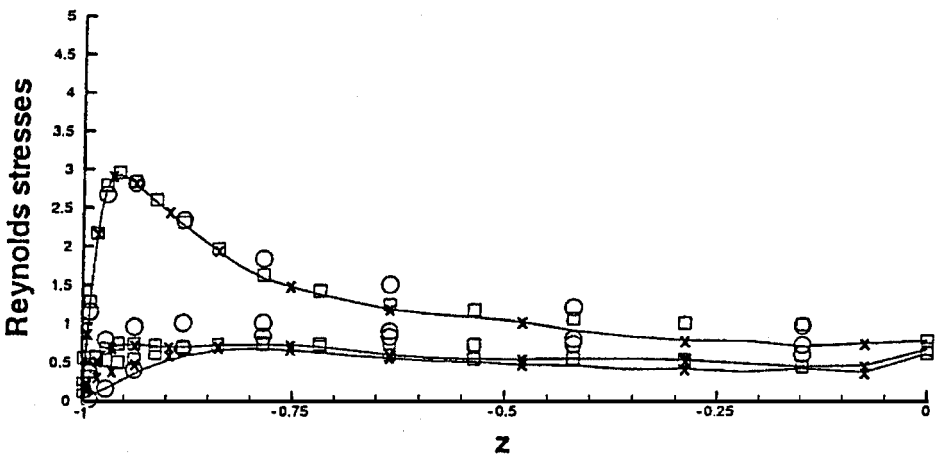

FIG. 10. Stationary channel computation, resolved Reynolds stresses. Circles, LES (case A1); solid line, hybrid (case B19); crosses, hybrid (case B18); squares, hybrid (case B13).

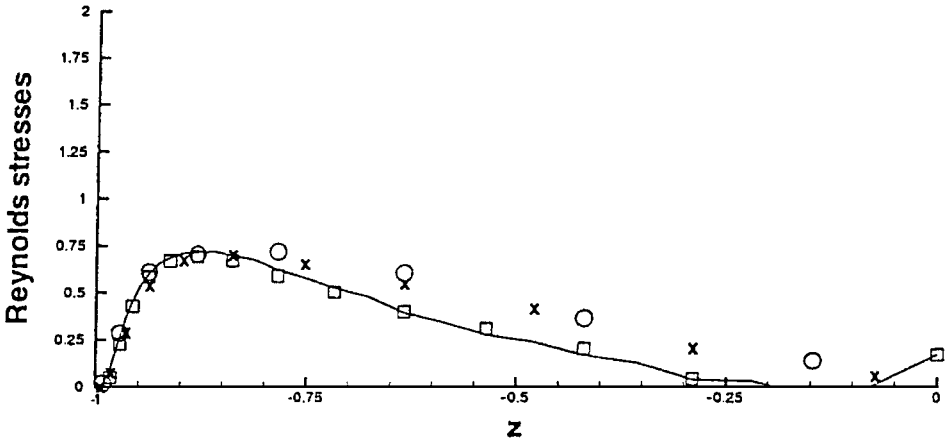

FIG. 11. Stationary channel computation, resolved shear stress. Circles, LES (case A1); solid line, hybrid (case B19); crosses, hybrid (case B18); squares, hybrid (case B13).

centerline. Even in the latter case, a spurious boundary layer was detected near the channel centerline.

In conclusion, the plane channel simulations have shown that (i) the hybrid approach makes it possible to maintain the accuracy of the simulation while using coarser grids than are used for classical LES (with $\Delta x^+ = 120$, $\Delta y^+ = 30$, and $\Delta z^+ = 5$ as a limit), (ii) the hybrid approach makes it possible to reduce the domain size to a halved minimal channel unit with a LES resolution and crude symmetry condition at the channel centerline, while keeping reliable results, and (iii) the hybrid approach is more robust than the classical LES approch.

The use of coarser meshes and a reduced computational domain resulted in significant CPU time saving with respect to classical LES on medium mesh and a full channel computational domain. Comparisons of CPU time and memory requirements are given in Table III. These two parameters are normalized by the equivalent requirement for classical LES on the medium mesh on the full channel domain (case A1). Experience shows that the gain is almost independent of the definition of the mean flow. The gain in CPU time in the case of Dom1 is induced by a faster convergence of the method for solving the Poisson equation.

5.4. Periodically Pulsed Plane Channel Flow

We now check the ability of the hybrid method to deal with unsteady mean flow and turbulence in strong disequilibrium. Previous NLDE computations [8] dealing with unsteady mean flow were restricted to 2D laminar cases. The pulse channel flow is chosen as a test

TABLE III
Comparison of CPU Costs and Memory Requirement

	Case						
	Dom1	Dom2	Dom3	Dom4	Dom5	Dom6	Dom7
CPU time	0.7	0.33	0.33	0.25	0.5	0.025	0.012
Memory	1	0.47	0.34	0.28	0.5	0.008	0.004

case. This flow has recently been studied numerically by Scotti and Piomelli [37]. The mean friction Reynolds number is still taken equal to 395. Computational parameters (mesh, domain size) are the same as for case A1. Following Refs. [30, 47], a sinusoidal forcing term is added in the streamwise direction of the momentum mean flow equations, which is equal to

$$f_i = A.U_{MAX}.\omega.\cos(\omega.t)\delta_{i1}, \tag{38}$$

where A is the forcing amplitude, U_{MAX} the value of the mean streamwise velocity on the centerline of the channel for the steady case, and ω the pulsating frequency, whose associated period is referred to as $T = 2\pi/\omega$.

The response of the flow to the unsteady forcing is characterized by the Stokes thickness l_s [30, 47],

$$l_s = \sqrt{\frac{\nu T}{\pi}}, \tag{39}$$

or, in wall units,

$$l_s^+ = \sqrt{\frac{T}{\pi\nu}}u_\tau. \tag{40}$$

For this type of flow, the amplitude A is known to be a less significant parameter than ω (or T) [44]. In order to minimize the duration of the computation while having strong unsteady effects, the parameter l_s^+ was chosen to be small, corresponding to a quickly oscillating mean flow. Several computations were studied, corresponding to different values of the Stokes thickness and the forcing amplitude. Computational parameters are summarized in Table IV. In each case, a classical LES computation and a simulation based on the proposed hybrid RANS/LES approach were perfomed.

The two selected values of the Stokes thickness correspond to different physical regimes. For $l_s^+ = 2.5$, the turbulence remains almost frozen during the whole forcing period [44], while in the second case the turbulence response is delayed with regard to the forced oscillations.

The time evolution of the unsteady $\langle\bar{u}\rangle$ field at two points ($z^+ = 1$ and 395) is shown in Figs. 12 and 13. As observed by many authors (see, for example, Refs. [30, 47]), a delay between the near-wall velocity response and the response of the velocity in the center of the channel (which corresponds to the forced oscillations) is observed. This delay decreases when l_s^+ increases. For the highest amplitudes ($A = 0.3$ and 0.5), the near-wall unsteady mean velocity $\langle\bar{u}\rangle$ becomes negative for quite a long time, which corresponds to recirculation. Time evolution of the friction Reynolds number is presented in Fig. 14. For C_2, C_3, and C_4 cases, the two discontinuities correspond to the occurence and the end of recirculation.

TABLE IV
Parameters of the Pulsed Channel Computations

	Case			
	C1	C2	C3	C4
l_s^+	2.5	2.5	2.5	8
A	0.1	0.3	0.5	0.3

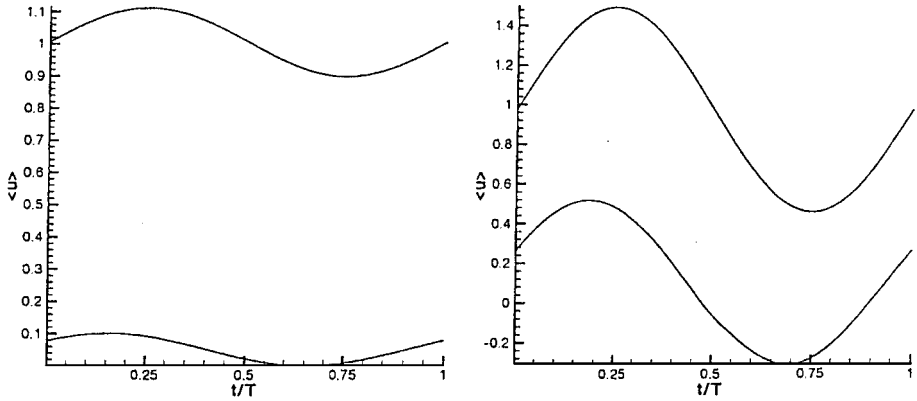

FIG. 12. Pulsed channel flow, time evolution of the mean flow velocity $\langle \bar{u} \rangle$. (Left) C1 case, (right) C3 case.

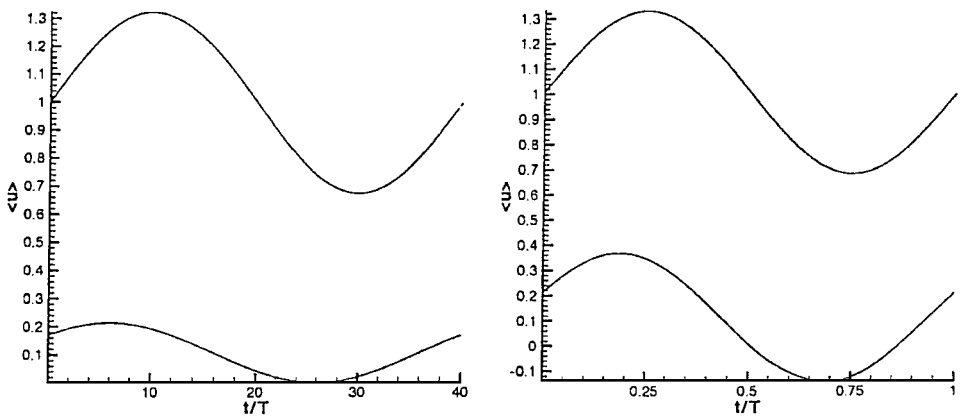

FIG. 13. Pulsed channel flow, time evolution of the mean flow velocity $\langle \bar{u} \rangle$. (Left) C2 case, (right) C4 case.

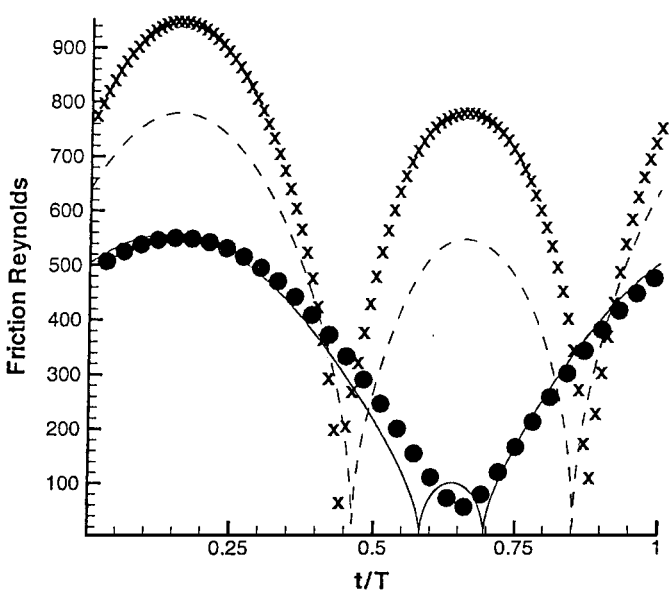

FIG. 14. Pulsed channel flow, time evolution of the friction Reynolds number Re_τ associated with the mean flow. ●, C1 case; dashed line, C2 case; ×, C3 case; solid line, C4 case.

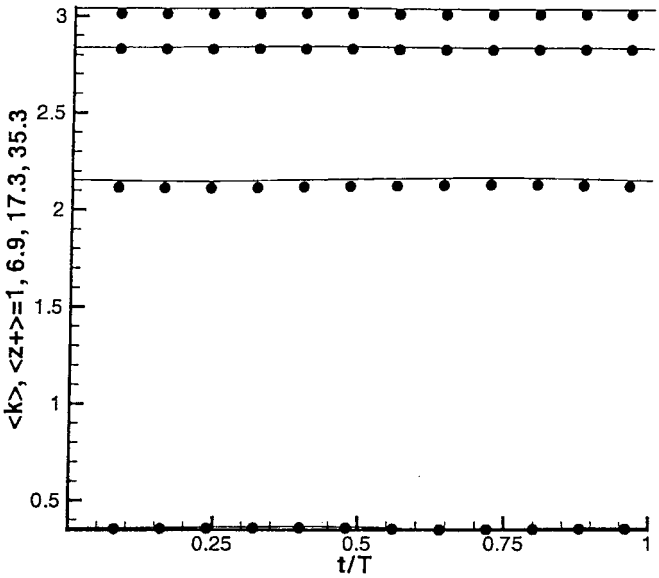

FIG. 15. Resolved turbulent kinetic energy, C1 case. Solid line, hybrid RANS/LES method; ●, LES.

Figures 15 to 18 compare the time evolution of the resolved turbulent kinetic energy obtained by the proposed method and a classical LES simulation at four positions. These positions correspond to $z^+ = 1$, 6.9, 17.3, and 35.3 with respect to the mean friction velocity. As expected, the high-frequency flow turbulence is almost frozen, while the low-frequency flow turbulence varies conspicuously. It is notable that the maximum turbulent kinetic energy for the last case is obtained during the deceleration of the flow, in good agreement with observations of previous authors. The agreement between classical LES and the hybrid approach is very satisfactory, with a relative maximum error of 5%.

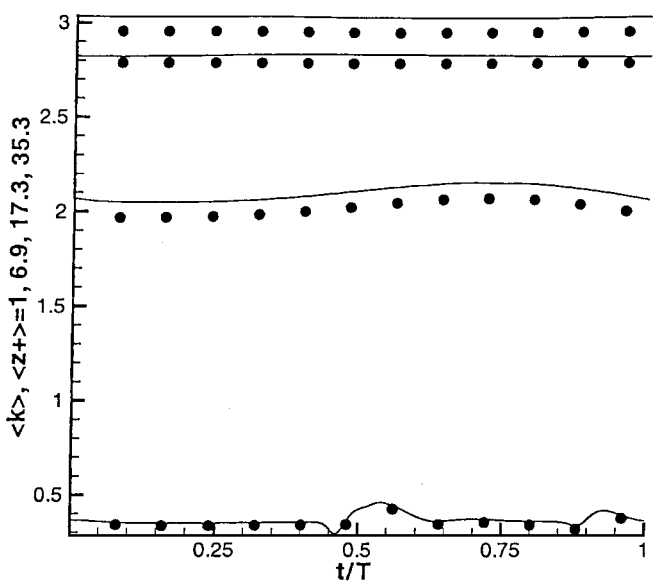

FIG. 16. Resolved turbulent kinetic energy, C3 case. Solid line, hybrid RANS/LES method; ●, LES.

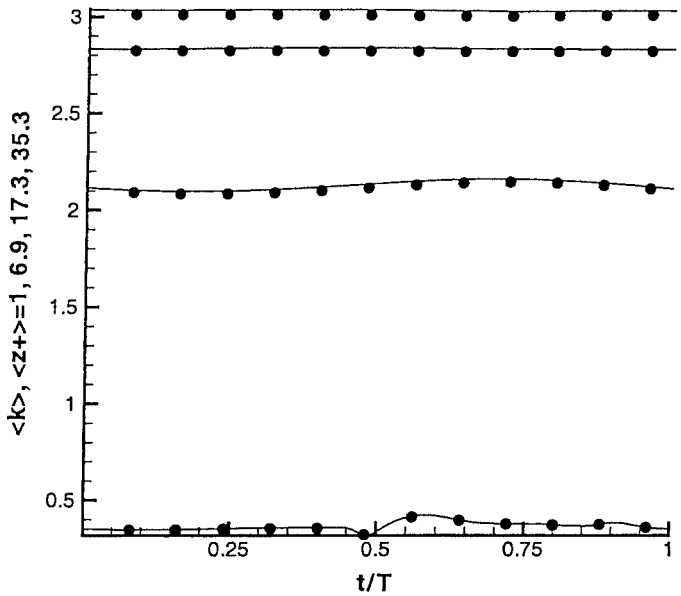

FIG. 17. Resolved turbulent kinetic energy, C2 case. Solid line, hybrid RANS/LES method; ●, LES.

Figures 19 to 26 show the resolved turbulent stresses at the beginning and at the half of the forcing period obtained by the presented method and by a classical LES calculation. In agreement with observations of previous authors, normalized Reynolds stress profiles do not vary in time for cases C1, C2, and C3, while they vary for the C4 case. A very good agreement between the two methods is observed, demonstrating the ability of the hybrid RANS/LES method to deal with statistically unsteady flows.

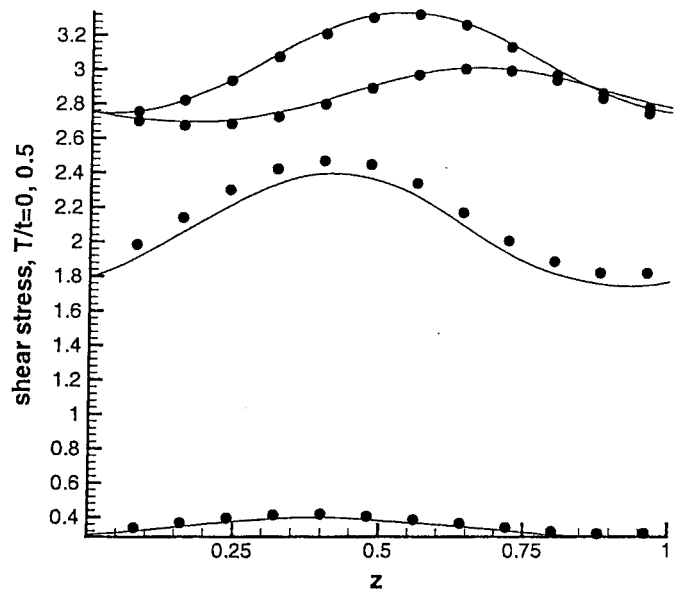

FIG. 18. Resolved turbulent kinetic energy, C4 case. Solid line, hybrid RANS/LES method; ●, LES.

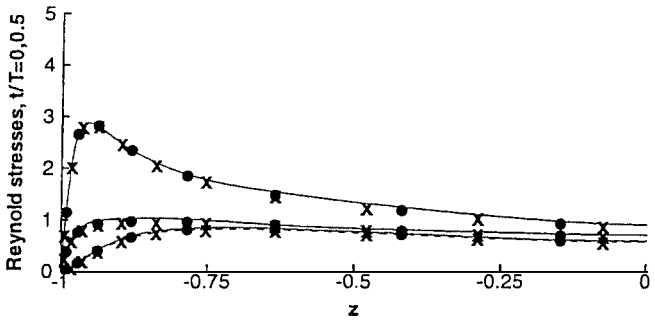

FIG. 19. Pulsed channel flow, C1 case, resolved Reynolds stresses: diagonal components. Solid line, hybrid RANS/LES method, $t/T = 0$; ●, LES, $t/T = 0$; dashed line, hybrid RANS/LES method, $t/T = 0.5$; ×, LES, $t/T = 0.5$.

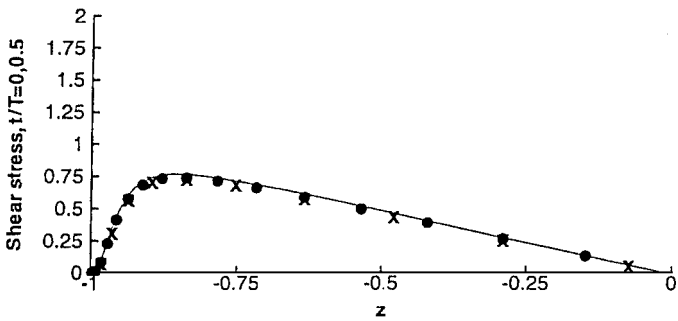

FIG. 20. Pulsed channel flow, C1 case, resolved Reynolds stresses: shear stress. Solid line, hybrid RANS/LES method, $t/T = 0$; ●, LES, $t/T = 0$; dashed line, hybrid RANS/LES method, $t/T = 0.5$; ×, LES, $t/T = 0.5$.

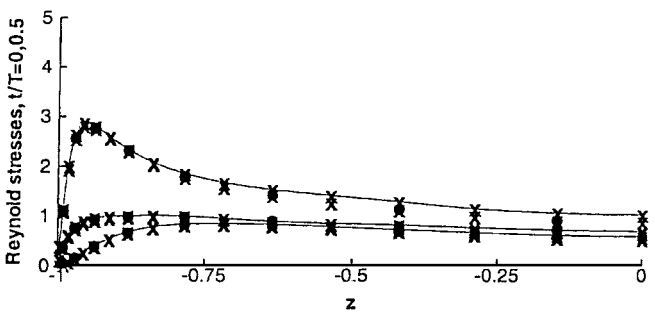

FIG. 21. Pulsed channel flow, C3 case, resolved Reynolds stresses: diagonal components. Solid line, hybrid RANS/LES method, $t/T = 0$; ●, LES, $t/T = 0$; dashed line, hybrid RANS/LES method, $t/T = 0.5$; ×, LES, $t/T = 0.5$.

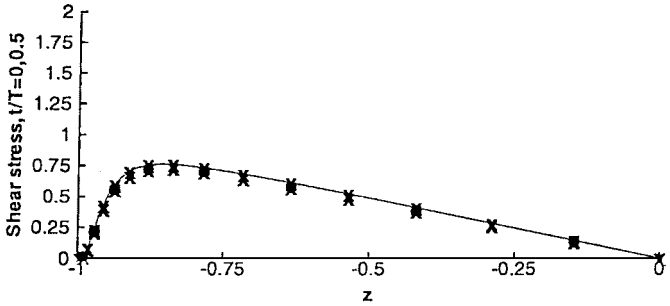

FIG. 22. Pulsed channel flow, C3 case, resolved Reynolds stresses: shear stress. Solid line, hybrid RANS/LES method, $t/T = 0$; ●, LES, $t/T = 0$; dashed line, hybrid RANS/LES method, $t/T = 0.5$; ×, LES, $t/T = 0.5$.

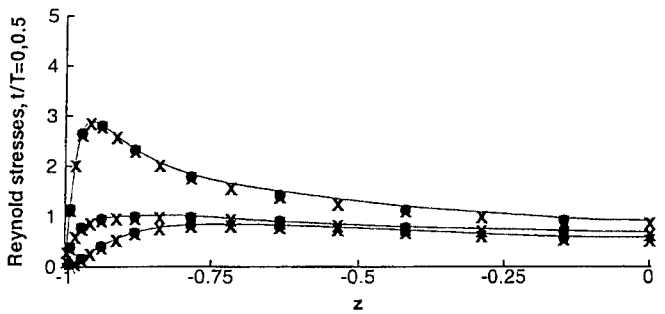

FIG. 23. Pulsed channel flow, C2 case, resolved Reynolds stresses: diagonal components. Solid line, hybrid RANS/LES method, $t/T = 0$; ●, LES, $t/T = 0$; dashed line, hybrid RANS/LES method, $t/T = 0.5$; ×, LES, $t/T = 0.5$.

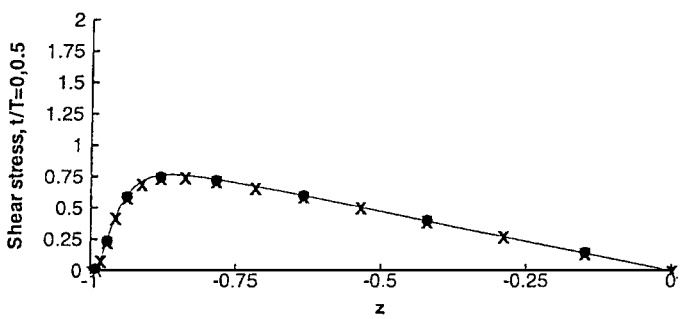

FIG. 24. Pulsed channel flow, C2 case, resolved Reynolds stresses: shear stress. Solid line, hybrid RANS/LES method, $t/T = 0$; ●, LES, $t/T = 0$; dashed line, hybrid RANS/LES method, $t/T = 0.5$; ×, LES, $t/T = 0.5$.

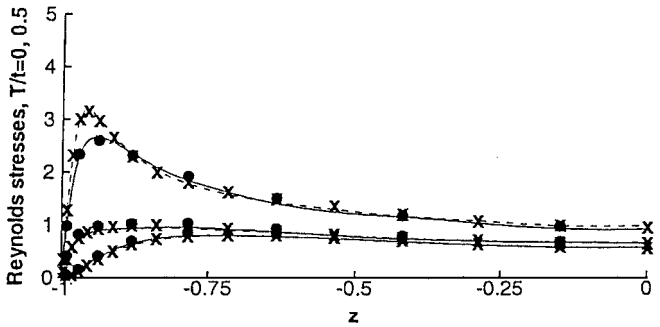

FIG. 25. Pulsed channel flow, C4 case, resolved Reynolds stresses: diagonal components. Solid line, hybrid RANS/LES method, $t/T = 0$; ●, LES, $t/T = 0$; dashed line, hybrid RANS/LES method, $t/T = 0.5$; ×, LES, $t/T = 0.5$.

6. APPLICATION TO THE FLOW AROUND A LOW-PRESSURE TURBINE BLADE

We now present results dealing with the application to a practical case: the flow around a low-pressure turbine blade. This flow exhibits many challenging features for the numerical prediction: transition to turbulence, vortex shedding, turbulent wake, separation ....

The T106 blade configuration is taken as a test case. The Reynolds number based on the chord and the inlet velocity is equal to 1.6×10^5. The Mach number is taken equal to 0.1. The inlet flow angle and the exit angle are equal to 37.7 and -63.2 degrees, respectively. The pitch-to-chord ratio is equal to 0.799. Previous classical LES calculations have already been carried out in this case [31].

The hybrid method is used to reconstruct the turbulent fluctuations both in the boundary layer and in the near wake. The gain with respect to the classical LES approach will come from the drastic reduction in the size of the computational domain.

6.1. Computational Parameters and Numerical Method

The mean flow is obtaind by carrying out a 2D steady RANS computation on the same mesh and in the same computational domain (in a $(x-y)$ plane) as is used for the LES [31]. The Spalart–Allmaras model [40] is used in the case. A steady solution is obtained using a finite-volume solver based on implicit time integration and a second-order-accurate

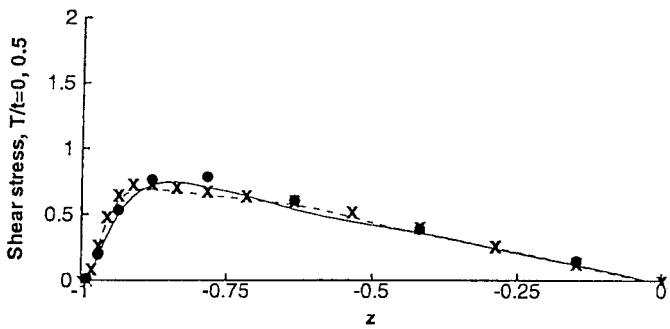

FIG. 26. Pulsed channel flow, C4 case, resolved Reynolds stresses: shear stress. Solid line, hybrid RANS/LES method, $t/T = 0$; ●, LES, $t/T = 0$; dashed line, hybrid RANS/LES method, $t/T = 0.5$; ×, LES, $t/T = 0.5$.

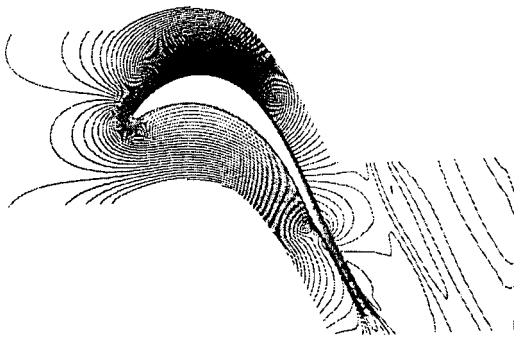

FIG. 27. Low-pressure turbine blade—isocontours of the Mach number of the RANS mean flow solution.

upwind TVD scheme. The Mach number distribution associated with the RANS solution is presented in Fig. 27. The present configuration was retained because the results are known to be very sensitive to the capture transition process. The Spallart–Allmaras model is seen to fail in predicting the existence of a separation bubble on the suction side near the trailing edge, because of the bad description of transition to turbulence on the suction side. As a consequence, the use of the coupled RANS/LES approach in this case is expected (i) to make it possible to get reconstructed fluctuations and (ii) to correct the mean flow distribution by capturing the separation bubble (iii) at lower costs than for classical LES of the same configuration.

The hybrid RANS/LES computations are performed in a subdomain containing the transition zone on the suction side of the blade, the trailing edge, and the near wake. Computational domains of LES, RANS, and hybrid RANS/LES computations are shown in Fig. 28. Classical LES and RANS computations are carried out using the whole computational domain, which is divided into several subdomains. Shadded subdomains correspond to the computational domain used to reconstruct fluctuations using the hybrid approach. Nonreflecting, characteristic boundary conditions are employed at the boundaries of the hybrid computation subdomain.

The same grid distribution is used for the hybrid computation as was used for the classical LES simulation. Along the blade, the grid is defined such that $\Delta x^+ < 40$, $\Delta z^+ < 10$. The first grid point away from the wall is such that $\Delta y^+ \leq 1$. The number of points per $(x–y)$ plane

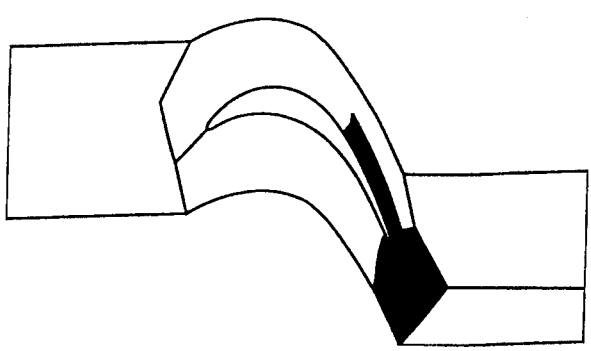

FIG. 28. Low-pressure turbine blade—RANS and LES computational domain. Shadded subdomains correspond to the hybrid simulation computational domain.

is then reduced from 90,644 (LES, full computational domain) to 26,306 (hybrid method, restricted computational domain). The spanwise extent of the domain is 3.2% of the chord in both cases. Thirty points are used in this direction, yielding $\Delta y^+ < 10$. The resolution is such that the simulation is a quasi-DNS in the transition region and behaves like a well-resolved LES in turbulent regions. Because of the deficiencies of the RANS computation and the need for a "healing" of the mean flow prediction in this case, and keeping in mind previous conclusions drawn from the plane channel flow simulation, this fine resolution was found to be necessary to get an accurate reconstruction of the fluctuations.

The numerical method and the subgrid model are the same for hybrid computations as for classical LES [31]. The Navier–Stokes equations are discretized using a cell-centered finite-volume approach on structured grid. A second-order-accurate numerical scheme is employed. Convective fluxes are discretized using a modified AUSM + (P) scheme, whose dissipation is controlled using a wiggle detector in order to render it adequate for LES [18]. Time integration is performed using a third-order-accurate compact Runge–Kutta scheme.

The cost of the hybrid simulation is one-third of that for the classical LES computation.

6.2. Results

Instantaneous views of the reconstructed fluctuations are shown in Figs. 29 and 30. Coherent structures near the trailing edge and in the wake are observed in Fig. 29, where a Schlieren-like view is presented. Isocontours of the instantaneous spanwise velocity component are plotted in Fig. 30 (subdomain boundaries are also shown). The hybrid simulation is seen to correctly predict the existence of vortex shedding and the structure of the wake. Transition from a 2D to a fully 3D flow is also seen to occur on the suction side of the blade before separation, in agreement with previous LES and experimental observations (see Ref. [31] for a discussion).

Mean flow profiles are compared in Fig. 31. It is seen that both LES and hybrid computations are in good agreement with experimental data because they are able to predict

FIG. 29. Low-pressure turbine blade—instantaneous view of the reconstructed fluctuating field (Schlieren-like representation).

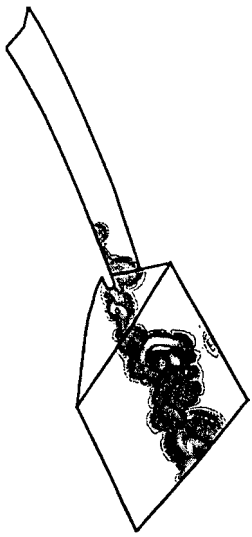

FIG. 30. Low-pressure turbine blade—instantaneous view of the reconstructed fluctuating field (spanwise velocity component).

the separation bubble on the suction side of the blade, while classical RANS fails. It is recalled that the difference between the RANS solution and the mean flow of the hybrid computation corresponds to the mean value of the reconstructed fluctuations. As in some previous channel flow computation with an unrealistic prescribed mean flow, the hybrid procedure is seen to be able to "heal" the mean flow deficiencies if a fine grid is used.

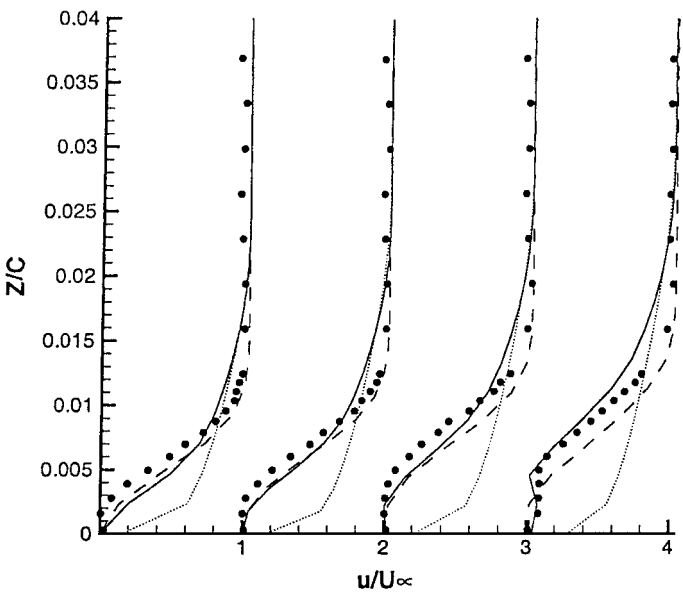

FIG. 31. Low-pressure turbine blade—computed mean velocity profile at different positions (70, 75, 80, and 85% of the chord) on the suction side. Experimental data: dashed line, classical LES; dotted line, RANS; solid line, hybrid computation.

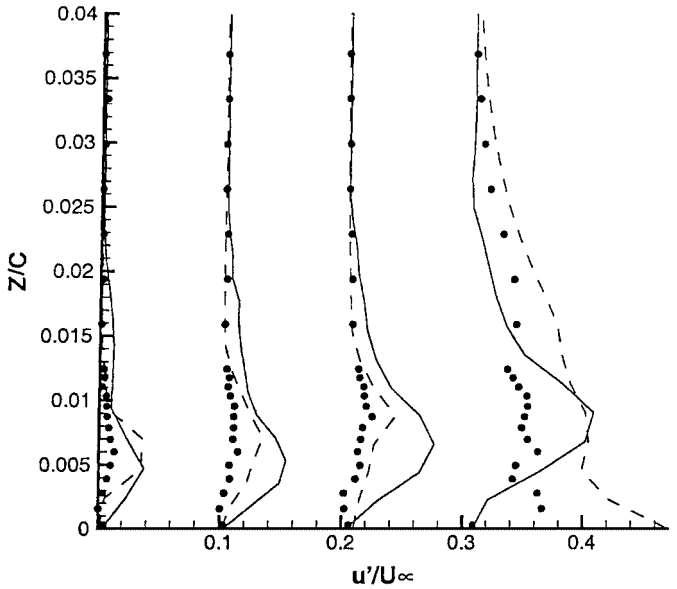

FIG. 32. Low-pressure turbine blade—computed rms streamwise velocity profile at different positions (70, 75, 80, and 85% of the chord) on the suction side. Experimental data: dashed line, classical LES; solid line, hybrid computation.

Computed streamwise turbulence intensity at several positions on the suction side of the blade are presented in Fig. 32. Similar profiles computed in the wake are shown in Fig. 33. Both classical LES and hybrid simulations are seen to yield qualitatively similar results. The overall level of error, compared to experimental results, is the same. Classical LES is observed to lead to a better prediction in the early stage of transition and separation, while

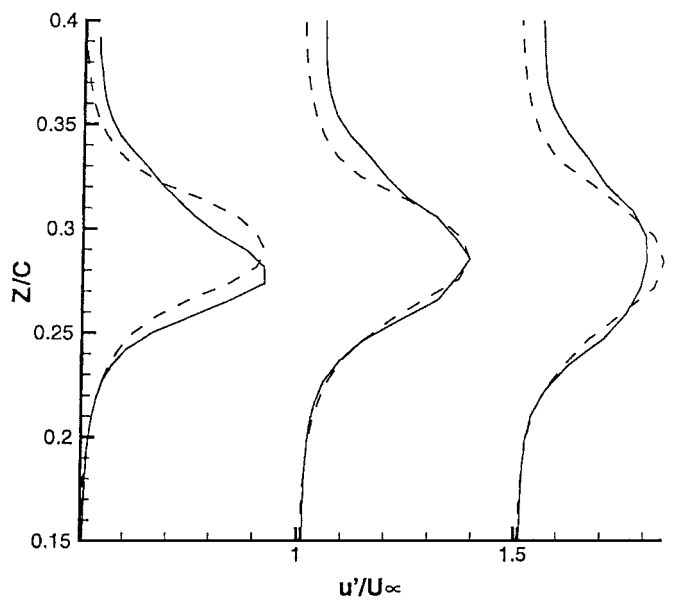

FIG. 33. Low-pressure turbine blade—computed rms streamwise velocity profile at different positions in the wake. Dashed line, classical LES; solid line, hybrid computation.

hybrid computation seems to yield a lower level of error during the last stage of transition. In the wake, results are very close, and both approaches predict the same maximal level of turbulent fluctuations.

7. CONCLUSIONS

A hybrid RANS/LES approach, relying on separate evalution of the mean flow field and the turbulent fluctuations, was proposed. The exact solution of the Navier–Stokes equations is split into three parts: mean flow, resolved fluctuations, and unresolved (subgrid) fluctuations. The means flow corresponds to the solution of a RANS-type problem, while resolved fluctuations are computed using a LES-like problem. Unresolved fluctuations are taken into account, thanks to a subgrid model. This hybrid approach corresponds to the most general extension of the NLDE approach, as defined by Morris and co-workers.

In the present paper, no simplification was used to derive the evolution equation for the fluctuations. This approach can be interpreted as a particular, three-level case of a general hierarchical scale-separation procedure. An associated theoretical framework has been introduced in the present paper, in both compressible and incompressible flow cases.

This coupled approach has been assessed on the stationary and the pulsed plane channel flow configuration. In both cases, the hybrid approach is observed to have the same accuracy as a usual LES simulation, when the same elements (numerical scheme, subgrid model, computational grid and computational domain, boundary conditions) are used. The results also demonstrate the robustness of the hybrid RANS/LES method with respect to several sources of error, such as grid resolution, the size of the computational domain, and some inconsistancies in the prescribed mean velocity profile. This improvement in the robustness can be explained by the fact that the separate definition of the mean velocity profile makes it easier to capture the turbulence production in the near-wall region.

It was also observed that when the prescribed mean velocity flow is not consistent with the mathematical model employed to describe the fluctuating flow, the use of the hybrid method makes it possible to recover corrections for the mean flow. But, in this case, the roubustness of the method with respect to the grid definition and the boundary conditions is expected to be the same as for the classical LES approach.

At last, the hybrid RANS/LES method was applied to compute the flow around a low-pressure turbine blade. This last application is a demonstration of the efficiency of the method on a realistic case. Here, the method was implemented in a structured multibloc compressible solver, and a challenging flow configuration was selected, where the hybrid simulation was also asked to alleviate some RANS computations problems.

It was also shown that the method can be used, even if the RANS computation and the hybrid computation are carried out using very different numerical methods.

APPENDIX 1: THE SPALART–ALLMARAS MODEL

The Spalart and Allmaras model [40] relies directly on a transport equation for the turbulent viscosity. The compressible form of this model leads to the following equations:

$$\mu_2 = \langle\rho\rangle \nu^* f_{v1}, \quad f_{v1} = \frac{\chi^3}{\chi^3 + c_{v1}^3}, \quad \chi = \frac{\nu^*}{\nu}. \tag{A.1}$$

The modified viscosity ν^* equals ν_2 away from the walls. The "damping function" f_{v1} is based on the well-known logarithmic law of the wall and lets ν_2 go smoothly to zero near the wall. A transport equation that applies to the modified viscosity ν^* is

$$\frac{\partial \nu^*}{\partial t} + \langle u \rangle \cdot \nabla \nu^* = \underbrace{c_{b1}(1 - f_{t2}) S^* \nu^*}_{\textit{Production}} + \underbrace{\frac{1}{P_{rtsa}} [\nabla \cdot ((\nu + \nu^*) \nabla \nu^*) + c_{b2} (\nabla \nu^*)^2]}_{\textit{Diffusion}} - \underbrace{\left[c_{w1} f_w - \frac{c_b 1}{\kappa^2} f_{t2} \right] \left(\frac{\nu^*}{d} \right)^2}_{\textit{Destruction}} + f_{t1} Du^2, \tag{A.2}$$

where S^* is related to the modified magnitude of the vorticity

$$S^* = |S| + \frac{\nu^*}{\kappa^2 d^2} f_{v2}, \quad f_{v2} = 1 - \frac{\chi}{1 + \chi f_{v1}}, \tag{A.3}$$

where $|S|$ is the magnitude of the vorticity and d the distance to the closest wall. The function f_{v2} is built, just like f_{v1}, on the hypothesis of a classical logarithmic-layer behavior. By the way, κ is the Karman constant, $\kappa \approx 0,41$.

The function f_w is used to recover the correct decay of the destruction term in the outer part of the boundary layer, and then to produce a realistic skin-friction coefficient:

$$f_w = g \left[\frac{1 + c_{w3}^6}{g^6 + c_{w3}^6} \right]^{1/6}, \quad g = r + c_{w2}(r^6 - r), \quad r = \frac{\nu^*}{S^* \kappa^2 d^2}. \tag{A.4}$$

The functions f_{t1} and f_{t2} are some trip functions which make it possible to prescribe the location of transition to turbulence,

$$f_{t2} = c_{t3} e^{-c_{t4} \chi^2}, \tag{A.5}$$

$$f_{t1} = c_{t1} g_t \exp\left(-c_{t2} \frac{\omega_t^2}{Du^2} \left[d^2 + g_t^2 d_t^2 \right] \right), \tag{A.6}$$

where d_t is the distance between the current point and the trip point, ω_t is the wall vorticity at the trip, Du is the difference between the velocity at the current point and that at the trip location, Δx_t is the grid spacing along the wall at the trip, and g_t is given by

$$g_t = \min\left(0.1, \frac{D_u}{\omega_t \Delta_{xt}} \right).$$

This model has demonstrated its efficiency in many industrial applications [1, 3, 32].

APPENDIX 2: THE $K - \varepsilon$ JONES–LAUNDER MODEL

The classical Jones–Launder $K - \varepsilon$ model used in the present study includes low Reynolds source terms [14]. The resulting equations for K and ε take the form

$$\frac{\partial K}{\partial t} + \nabla \cdot (\langle \bar{u} \rangle K) = \nabla \cdot \left[\left(\mu + \frac{\mu_2}{\alpha_k} \right) \nabla K \right] + \tau_R : \nabla \langle \bar{u} \rangle - \varepsilon - 2\mu (\nabla \sqrt{K})^2, \tag{A.7}$$

$$\frac{\partial \varepsilon}{\partial t} + \nabla \cdot (\langle \bar{u} \rangle \varepsilon) = \nabla \cdot \left[\left(\mu + \frac{\mu_2}{\alpha_\varepsilon} \right) \nabla \varepsilon \right] + C_1 f_1 \frac{\varepsilon}{K} \tau_R : \nabla \langle \bar{u} \rangle - C_2 f_2 \frac{\varepsilon^2}{K} + 2\mu\mu_2 \left(\frac{\partial^2 \langle \bar{u} \rangle}{\partial n^2} \right)^2, \quad \text{(A.8)}$$

where n represents the unit-normal vector to the considered wall and τ_R is computed using the eddy–viscosity hypothesis:

$$\tau_R = -\frac{2}{3} K Id + \mu_2 (\nabla \langle \bar{u} \rangle + \nabla^T \langle \bar{u} \rangle). \quad \text{(A.9)}$$

Then, the turbulent viscosity can be obtained by

$$\mu_2 = C_\mu \frac{K^2}{\varepsilon} \exp \left[\frac{-2.5}{1 + \frac{R_t}{50}} \right], \quad \text{(A.10)}$$

where $R_t = K^2/\mu\varepsilon$ is the turbulent Reynolds number.

The constants of the model take classical values: $\alpha_k = 1$, $\alpha_\varepsilon = 1.3$, $C_1 = 1.55$, $C_2 = 2$, $f_1 = 1$, $f_2 = 1 - 0.3 \exp(-R_t^2)$, $C_\mu = 0.09$.

APPENDIX 3: LES CLOSURE

The subgrid-scale viscosity μ_1 is computed using the selective mixed scale model [29, 33, 35],

$$\mu_1 = C f_{\theta_0}(\theta) |\bar{\omega}^1|^{\frac{1}{2}} \Delta^{\frac{3}{2}} q_c^{\frac{1}{2}}, \quad \text{(A.11)}$$

where $\bar{\omega}^1 = \nabla \times \bar{u}^1$ and $C = 0.06$. The local value of cutoff length Δ is assumed to be equal to the cubic root of the volume of the corresponding grid cell. The resolved high-frequency kinetic energy is computed as

$$q_c^2 = \frac{1}{2} (\widetilde{\bar{u}^1} - \bar{u}^1)^2,$$

where the test velocity field $\widetilde{\bar{u}^1}$ is evaluated by applying a three-point-stencil discrete test filter to $\bar{u}^1$. The selection function $f_{\theta_0}(\theta)$ is defined as [33, 35]

$$\theta = \arcsin \left(\frac{\| \widetilde{\bar{\omega}^1} \otimes \bar{\omega}^1 \|}{\| \widetilde{\bar{\omega}^1} \| \cdot \| \bar{\omega}^1 \|} \right), \quad \text{(A.12)}$$

$$f_s(\theta_0) = \begin{cases} 1, & \text{if } \theta > \theta_0, \\ \tau^n(\theta), & \text{otherwise}, \end{cases} \quad \text{(A.13)}$$

with $\theta_0 = 20^\circ$ and $n = 2$ in present computations. Function $\tau(\theta)$ is defined as

$$\tau(\theta) = \frac{\tan^2 \left(\frac{\theta}{2} \right)}{\tan^2 \left(\frac{\theta_0}{2} \right)}. \quad \text{(A.14)}$$

ACKNOWLEDGMENTS

B. Raverdy is acknowledged for providing LES results on the low-pressure turbine blade configuration. I. Mary provided useful help during the implementation of NLDE. RANS results on the low-pressure turbine blade were kindly provided by S. Deck.

REFERENCES

1. W. K. Anderson and D. L. Bonhaus, *Navier-Stokes Computations and Experimental Comparisons for Multi-element airfoil Configurations*, AIAA Paper 93-0645 (1993).
2. T. Chyczewski, P. Morris, and L. Long, *Large-Eddy Simulation of Wall Bounded Flow Using the Nonlinear Disturbance Equations*, AIAA Paper 2000-2007 (2000).
3. S. Deck, R. Hallard, and P. Guillen, *Numerical Simulation of Steady and Unsteady Separated Nozzle Flows*, AIAA Paper 02-0406 (2002).
4. T. Dubois, F. Jauberteau, and R. Temam, Incremental unknowns, multilevel methods and the numerical simulation of turbulence, *Comput. Methods Appl. Mech. Engr.* **159**, 123 (1998).
5. M. Germano, From RANS to DNS: Towards a bridging model, in *Direct and Large Eddy Simulation III*, edited by P. R. Voke, N. D. Sandham, and L. Kleiser (Kluwer Academic, Dordrecht/Norwall, MA, 2000), p. 225.
6. M. Germano, A statistical formulation of the dynamic model, *Phys. Fluids* **8**(2), 565 (1996).
7. S. Ghosal and P. Moin, The basic equations for the large-eddy simulation of turbulent flows in complex geometries, *J. Comput. Phys.* **118**, 24 (1995).
8. R. P. Hansen, L. N. Long, and P. J. Morris, *Unsteady, Laminar Flow Simulations Using the Nonlinear Disturbance Equations*, AIAA Paper 2000-1981 (2000).
9. A. Harten, Multiresolution of data: A general framework, *SIAM J. Numer. Anal.* **33**(3), 1205 (1996).
10. J. Jimenez and P. Moin, The minimal flow unit in near-wall turbulence, *J. Fluid Mech.* **225**, 213 (1991).
11. J. Jimenez and A. Pinelli, The autonomous cycle of near-wall turbulence, *J. Fluid Mech.* **389**, 335 (1999).
12. J. Jimenez and M. P. Simens, Low-dimensional dynamics of a turbulent wall flow, *J. Fluid Mech.* **435**, 81 (2001).
13. J. Jimenez and C. Vasco, Approximate lateral boundary conditions for turbulent simulations in *Proceedings of the 1998 Summer program* (Center for Turbulence Research, NASA Ames/Stanford Univ., Stanford, CA, 1998), p. 399.
14. W. P. Jones and B. E. Launder, The calculation of low-Reynolds-number phenomena with a two-equation model of turbulence, *J. Heat Mass Transfer* **16**, 1119 (1973).
15. M. Korrami and B. Singer, *Stability Analysis for Noise-Source Modeling of a Part-Span Flap*, AIAA Paper 98-2225 (1998).
16. M. Lesieur and O. Metais, New trends in large-eddy simulations of turbulence, *Annu. Rev. Fluid Mech.* **28**, 45 (1996).
17. E. Longatte, P. Lafon, and S. Candel, Computation of acoustic propagation in two-dimensional sheared ducted flows, *AIAA J.* **38**(3), 389 (2000).
18. I. Mary and P. Sagaut, Large-eddy simulation of the flow around a profile near stall, *AIAA J.* **36**(1), 1139 (2002).
19. C. Meneveau and J. Katz, Scale-invariance and turbulence models for large-eddy simulation, *Annu. Rev. Fluid Mech.* **32**, 1 (2000).
20. P. J. Morris, L. N. Long, A. Bangalore, and Q. Wang, A parallel three-dimensional computational aeroacoustics method using nonlinear disturbance equations, *J. Comput. Phys.* **133**, 56 (1997).
21. P. J. Morris, L. N. Long, Q. Wang, and D. P. Lockard, *Numerical Prediction of High-Speed Jet Noise*, AIAA Paper 97-1598 (1997).
22. P. J. Morris, L. N. Long, Q. Wang, and A. R. Pilon, *High-Speed Jet Noise Simulations*, AIAA Paper 98-2290 (1998).

23. R. D. Moser, J. Kim, and N. N. Mansour, DNS of turbulent channel flow up to $Re_\tau = 590$, *Phys. Fluids* **11**, 943 (1999).
24. F. Nicoud, G. Winckelmans, D. Carati, J. Baggett, and W. Cabot, Boundary conditions for LES away from the wall, in *Proceedings of the 1998 Summer program* (Center for Turbulence Research, NASA Ames/Stanford Univ., Stanford, CA, 1998), p. 413.
25. A. Pascarelli and U. Piomelli, Multiblock simulations of turbulent boundary layers, *J. Comput. Phys.* **157**, 256 (1999).
26. J. Piquet, *Turbulence Flows, Models and Physics* (Springer-Verlag, Berlin/New York, 1999).
27. C. D. Pruett, Eulerian time-domain filtering for spatial large-eddy simulation, *AIAA J.* **38**(9), 1634 (2000).
28. P. Quéméré and P. Sagaut, Zonal multidomain RANS/LES simulations of turbulent flows, *Int. J. Numer. Methods Fluids*, in press.
29. P. Quéméré, P. Sagaut, and V. Couaillier, A new multidomain/multiresolution technique for large-eddy simulation, *Int. J. Numer. Methods Fluids* **36**, 391 (2001).
30. B. R. Ramaprian and S. W. Tu, Fully developed periodic turbulent pipe flow. Part 2. The detailed structure of the flow, *J. Fluid Mech.* **137**, 31 (1983).
31. B. Raverdy, L. Mary, P. Sagaut, and N. Liamis, Large-eddy simulation of the transitional flow around a low-pressure turbine blade, in *Direct and Large-eddy simulation IV*, edited by B. J. Geurts, R. Friedric, and O. Métais (Kluwer Academic Publishers, Dordrecht, The Netherlands, 2001), p. 381.
32. C. L. Rumsey and V. N. Vatsa, *A Comparison of the Predictive Capabilities of Several Turbulence Models Using Upwing and Central-Difference Computer Codes*, AIAA Paper 93-0645 (1993).
33. P. Sagaut, *Large-Eddy Simulation for Incompressible Flows—An Introduction* (Springer-Verlag, Berlin/ New York, 2001).
34. P. Sagaut, E. Labourasse, P. Quéméré, and M. Terracol, Multiscale approaches to unsteady simulation of turbulent flows, *Int. J. Nonlinear Sci. Numer. Simulation* **1**, 285 (2000).
35. P. Sagaut, E. Montreuil, and O. Labbé, Assessment of some self-adaptive SGS models for wall bounded flows, *Aerospace Sci. Technol.* **3**(6), 335 (1999).
36. U. Schumann, Subgrid scale model for finite difference simulations in plane chanels and annuli, *J. Comput. Phys.* **18**, 376 (1975).
37. A. Scotti and U. Piomelli, Numerical simulation of pulsating turbulent channel flow, *Phys. Fluids* **13**(5), 1367 (2001).
38. L. Shao, S. Sarkar, and C. Pantano, On the relationship between the mean flow and subgrid stresses in large eddy simulation of turbulent shear flows, *Phys. Fluids* **11**(5), 1229 (1999).
39. S. A. Slimon, M. C. Soteriou, and D. W. Davis, Computational aeroacoustics simulations using the expansion about incompressible flow approach, *AIAA J.* **37**(4), 409 (1999).
40. P. R. Spalart and S. R. Allmaras, *A One-Equation Model for Aerodynamic Flows*, AIAA Paper 92-0439 (1992).
41. P. R. Spalart, W.- H. Jou, M. Strelets, and S. R. Almaras, Comments on the feasibility of LES for wings, and on a hybrid RANS/LES approach, in *Advances in DNS/LES*, edited by C. Liu and Z. Liu (Greyden Press, Colombus, 1998), p. 137.
42. C. G. Speziale, Turbulence modeling for time-dependent RANS and VLES: A review, *AIAA J.* **36**(2), 173 (1998).
43. C. L. Streett, *Numerical Simulation of Fluctuations Leading to Noise in a Flap-Edge Flowfield*, AIAA Paper 98-628 (1998).
44. S. Tardu and G. Binder, Wall shear stress modulation in unsteady turbulent channel flow with high imposed frequencies, *Phys. Fluids* **5**, 2028 (1993).
45. M. Terracol, P. Sagaut, and C. Basdevant, Une méthode multiniveau pour la simulation des grandes échelles des écoulements turbulents compressibles, *C. R. Acad. Sci. Paris Sér. IIb* **328**, 81 (2000).
46. M. Terracol, P. Sagaut, and C. Basdevant, A multilevel algorithm for large-eddy simulation of turbulent compressible flows, *J. Comput. Phys.* **167**, 439 (2001).
47. S. W. Tu and B. R. Ramaprian, Fully developed periodic turbulent pipe flow. Part 1. Main experimental results and comparison with predictions, *J. Fluid Mech.* **137**, 31 (1983).

48. O. V. Vasyliev, T. S. Lund, and P. Moin, A general class of commutative filters for LES in complex geometries, *J. Comput. Phys.* **146**, 82 (1998).
49. K. Viswanathan and L. N. Sankar, Toward the direct calculation of noise: Fluid/acoustic coupled simulation, *AIAA J.* **33**(12), 2271 (2000).
50. B. Vreman, *Direct and Large-Eddy Simulation of the Compressible Mixing Layer*, Ph.D. thesis (Twente University, Twente, The Netherlands, 1995).
51. F. Waleffe, Exact coherent structures in channel flow, *J. Fluid Mech* **435**, 93 (2001).
52. S. Zahrai, F. H. Bark, and R. I. Karlsson, On anisotropic subgrid modeling, *Eur. J. Mech. B* **14**(4), 459 (1995).
53. Y. Zang, Numerical simulation of the dynamics of turbulent boundary layers: Perspectives of a transition simulator, *Philos. Trans. R. Soc. London Ser. A* **336**, 95 (1991).